Paleoceanography and Paleoclimatology

RESEARCH ARTICLE
10.1029/2018PA003425

Widespread Warming Before and Elevated Barium Burial During the Paleocene-Eocene Thermal Maximum: Evidence for Methane Hydrate Release?

J. Frieling[1], F. Peterse[2], D. J. Lunt[3], S. M. Bohaty[4], J. S. Sinninghe Damsté[2,5], G. -J. Reichart[2,6], and A. Sluijs[1]

[1]Marine Palynology and Paleoceanography, Laboratory of Palaeobotany and Palynology, Department of Earth Sciences, Faculty of Geosciences, Utrecht University, Utrecht, The Netherlands, [2]Department of Earth Sciences, Faculty of Geosciences, Utrecht University, Utrecht, The Netherlands, [3]School of Geographical Sciences, University of Bristol, Bristol, UK, [4]Ocean and Earth Science, National Oceanography Centre Southampton, University of Southampton, Waterfront Campus, Southampton, UK, [5]NIOZ Royal Netherlands Institute for Sea Research, Department of Marine Microbiology and Biogeochemistry, and Utrecht University, Texel, The Netherlands, [6]NIOZ Royal Netherlands Institute for Sea Research, Department of Ocean Sciences, and Utrecht University, Texel, The Netherlands

Key Points:
- Global sea surface warming (2 degree Celsius) is shown to lead the PETM carbon isotope excursion based on new and published high-resolution records
- Compiled Ba data show oceanic Ba burial rates rose by a factor of 3 on average, supporting a large additional source of Ba during the PETM
- The above observations may be explained by dissociation of submarine methane hydrates, triggered by an early warming

Supporting Information:
- Supporting Information S1
- Data Set S1
- Data Set S2

Correspondence to:
J. Frieling,
j.frieling1@uu.nl

Citation:
Frieling, J., Peterse, F., Lunt, D. J., Bohaty, S. M., Sinninghe Damsté, J. S., Reichart, G. -J., & Sluijs, A. (2019). Widespread warming before and elevated barium burial during the Paleocene-Eocene Thermal Maximum: Evidence for methane hydrate release?. *Paleoceanography and Paleoclimatology*, *34*, 546–566. https://doi.org/10.1029/2018PA003425

Received 8 JUL 2018
Accepted 8 MAR 2019
Accepted article online 18 MAR 2019
Published online 17 APR 2019

Abstract Current climate change may induce positive carbon cycle feedbacks that amplify anthropogenic warming on time scales of centuries to millennia. Similar feedbacks might have been active during a phase of carbon cycle perturbation and global warming, termed the Paleocene-Eocene Thermal Maximum (PETM, 56 million years ago). The PETM may help constrain these feedbacks and their sensitivity to warming. We present new high-resolution carbon isotope and sea surface temperature data from Ocean Drilling Program Site 959 in the Equatorial Atlantic. With these and existing data from the New Jersey Shelf and Maud Rise, Southern Ocean, we quantify the lead-lag relation between PETM warming and the carbon input that caused the carbon isotope excursion (CIE). We show ~2 °C of global warming preceded the CIE by millennia, strongly implicating CO_2-driven warming triggered a positive carbon cycle feedback. We further compile new and published barium (Ba) records encompassing continental shelf, slope, and deep ocean settings. Based on this compilation, we calculate that average Ba burial rates approximately tripled during the PETM, which may require an additional source of Ba to the ocean. Although the precipitation pathway is not well constrained, dissolved Ba stored in sulfate-depleted pore waters below methane hydrates could represent an additional source. We speculate the most complete explanation for early warming and rise in Ba supply is that hydrate dissociation acted as a positive feedback and caused the CIE. These results imply hydrates are more temperature sensitive than previously considered, and may warrant reconsideration of the political assignment of 2 °C warming as a safe future scenario.

1. Introduction

The Paleocene-Eocene Thermal Maximum (PETM) is an extensively studied period of rapid global warming (4–5 °C; Dunkley Jones et al., 2013; Frieling et al., 2017), associated with a substantial (>1,500 Gt) carbon input from a ^{13}C-depleted carbon source into the ocean-atmosphere system (Dickens et al., 1995) with a sufficient quantity and rate to acidify the oceans (Babila et al., 2016; Penman et al., 2014; Zachos et al., 2005). The input of ^{13}C-depleted carbon at the onset of the PETM is globally recognized in both sedimentary carbonate and organic matter as a negative carbon isotope excursion (CIE; e.g., McInerney & Wing, 2011). The CIE is characterized by a rapid (millennial scale; Zeebe et al., 2016) onset of ~3–5‰, a phase of low stable carbon isotope ratio ($\delta^{13}C$) values (often referred to as "body"), and a more gradual recovery (e.g., McInerney & Wing, 2011). A similar pattern is recorded by temperature proxies (Dunkley Jones et al., 2013), suggesting a close connection between temperature and the CIE. Release of thermogenic methane may explain at least part of the CIE body based on direct dating of outgassing from a vent system in the North Atlantic (Frieling et al., 2016). Still, the onset of the CIE might have been caused by other vents and/or carbon cycle feedbacks such as methane hydrate release (Dickens et al., 1995) or organic matter oxidation (DeConto et al., 2012; Kurtz et al., 2003). Despite earlier exclusion of a volcanic source (Dickens, 2001a), Gutjahr et al. (2017) suggested based on an inverse modeling exercise that volcanic outgassing may explain the entire CIE. While specific carbon sources have been shown to actively contribute to the CIE (Frieling et al., 2016; Lyons et al., 2019), none of the sources have been confidently tied to the onset of

the CIE using stratigraphic, proxy tracers or field data. Indeed, some sources, such as terrestrial organic matter oxidation, may be exceptionally difficult to trace in the geological record.

Along with the PETM, carbon isotope and deep sea carbonate deposition patterns show clear evidence of orbitally paced variability throughout Paleocene and early Eocene records, some of which is accompanied by temperature anomalies that have been termed "hyperthermals" (Lauretano et al., 2015, 2016; Littler et al., 2014; Zachos et al., 2010). These include Eocene Thermal Maximum 2 (also termed H1; Lourens et al., 2005), Eocene Thermal Maximum 3 (also termed X or K, Agnini et al., 2009), the Latest Danian Event (Bornemann et al., 2009; Deprez et al., 2017), and Lower Chron 26r (L. C26r) event (Coccioni et al., 2012). The clear orbital pacing of these events suggest a climatic trigger for ^{13}C-depleted carbon input (Lauretano et al., 2015; Littler et al., 2014; Lourens et al., 2005). The PETM is the largest of these events and of a much longer duration, and the latest age models suggest that it was out of phase with maxima in the 400-kyr cycle (Littler et al., 2014; Westerhold et al., 2017) unlike many of the other hyperthermals. This suggests the PETM was an anomalous event even in the context of the orbitally paced hyperthermals of the early Paleogene, although it is still difficult to exclude orbital factors in its cause.

Previous work has suggested that surface warming preceded the PETM CIE at several locations in the mid and high latitudes, perhaps suggesting a global signal (Chen et al., 2014; Secord et al., 2010; Sluijs et al., 2007; Thomas et al., 2002). If this warming was global in nature, the most likely cause was a rise in CO_2 prior to the onset of the CIE although information on CO_2 is currently lacking. Alternatively, if warming was restricted to mid- and high-latitude regions it may indicate a change in ocean circulation patterns associated with astronomical forcing superimposed on the long-term late Paleocene warming trend (Lunt et al., 2011). In either case, a synchronous widespread pre-CIE warming would imply the CIE likely resulted from a positive carbon cycle feedback like permafrost thawing (DeConto et al., 2012) or methane hydrate dissociation (Dickens et al., 1995; Lunt et al., 2011). In contrast, if no distinct pattern in lead-lag relations between warming and the onset of the CIE is evident, the first injected carbon likely caused both.

Another parameter that is potentially of interest for deducing carbon sourcing during the PETM is barium (Ba) burial fluxes. Previous work (Ma et al., 2014; Paytan et al., 2007) observed a substantial increase in Ba burial in the deep sea, which necessitates an increase in Ba supply to the open ocean. Despite the absence of Ba data from shelf or slope settings, Paytan et al. (2007) hypothesized that the additional Ba supply to the deep sea originated from shelf regions. This hypothesis relies on Ba remobilization under low-oxygen conditions, which become more prevalent during the PETM (e.g., Dickson et al., 2012). Alternatively, Dickens et al. (2003) showed that pore waters below methane hydrates store large amounts of dissolved Ba and therefore methane hydrate dissociation should produce a transient increase in the total input of dissolved Ba into the global ocean. Collectively, the methane hydrate hypothesis therefore requires pre-CIE warming as well as an average increase in Ba burial, across continental shelves, slopes, and deep oceans.

To resolve these issues, we generated new high-resolution Total Organic Carbon (TOC) $\delta^{13}C$ data ($\delta^{13}C_{TOC}$), the TetraEther indeX of tetraethers consisting of 86 carbon atoms (TEX_{86}) sea surface temperature (SST) and inorganic geochemical data from Ocean Drilling Program (ODP) Site 959, located in the equatorial Eastern Atlantic near the top of a submarine high, the Cote d'Ivoire Ghana Transform Margin (CIGTM; 3°37.656′N, 2°44.149′W; Figure 1). The new results are placed in a global context using high-resolution temperature-$\delta^{13}C$ data from Wilson Lake and Bass River on the New Jersey Shelf (Sluijs et al., 2007) and ODP Sites 689 and 690 on Maud Rise, Weddell Sea (Kennett & Stott, 1991; Thomas et al., 2002; Zachos et al., 2007). Time lags between warming and the CIE are evaluated using cross-correlation functions (ccfs). Furthermore, we extend the global barium burial data set with published and newly generated data to increase coverage of different oceanographic settings in shelf, slope, and deep ocean settings.

2. Methods

2.1. Materials

Site 959 was drilled on the CIGTM in 1995 (3°37.656′N, 2°44.149′W; Figure 1). Nannoplankton biostratigraphy indicates the presence of the late Paleocene and early Eocene CP8a-CP8b Zone boundary in the interval from Section 959D-41R-6 to Section -42R-2 (Shafik et al., 1998). We continuously sampled Sections 959D-41R-6, -41R-CC, -42R-1, and -42R-2., representing the interval from 800.5 to 805.58 meters below sea floor

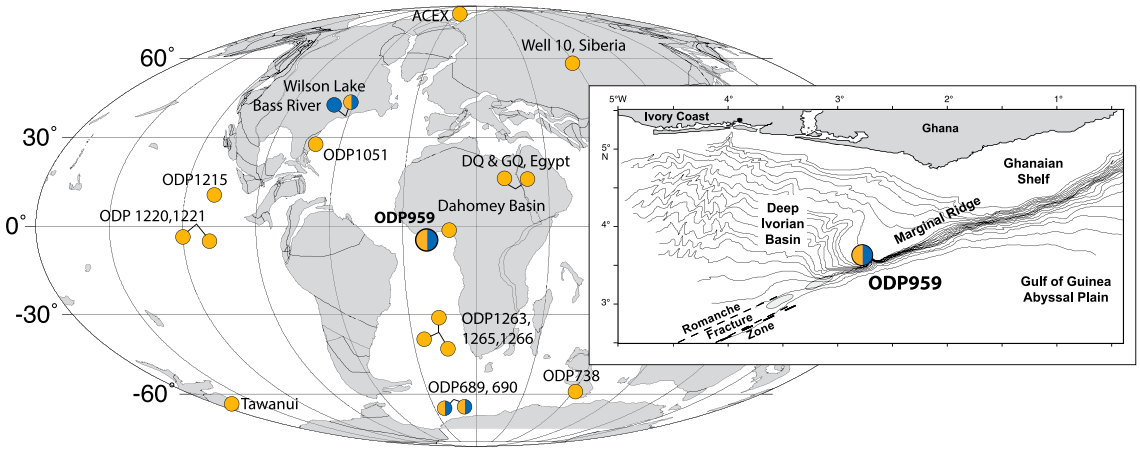

Figure 1. Locations for all sites used in this study, plate reconstruction for 56 million years ago (Ma). Site coloring; blue indicates sites used in lead-lag analyses, yellow indicates sites used in barium burial compilation. We present new data for ODP Site 959, Dahomey Basin and Well 10—Siberia. Insert: modern location of Site 959 and primary bathymetric features. IODP = International Ocean Discovery Program; ODP = Ocean Drilling Program; DQ = Dababiya Quarry; GQ = Gabal al Qreiya.

(mbsf) at a resolution of 1–3 cm. Between Cores 959D-41R and -42R there is a core gap of ~1 m. Notable lithological changes occur in the interval from 804.1 to 803.9 mbsf, where porcellanite is present and likely represents recrystallization of biosiliceous sediments. (Shipboard Science Party, 1996). The sediments above Core 959D-41R-6 are recognized by more frequent occurrences of porcellanite (Shipboard Science Party, 1996; Wagner, 2002). Sediments below Section 959D-42R-1 show apparently cyclic dark-light alterations, representing variable amounts of clay, carbonate, organic matter, and biogenic silica (Wagner, 2002).

The tectonic evolution of the CIGTM implies that Site 959 has been located at >1,000 m water depth since the Maastrichtian (Oboh-Ikuenobe et al., 1997). Site 959 is considered to be above the calcite compensation depth (CCD) during the entire interval.

2.2. Methods and Data Quality Assessment

2.2.1. $\delta^{13}C_{TOC}$ and Age Model

Approximately 0.3 g of freeze-dried material was powdered and subsequently decarbonated using two steps of 1 M HCl. The residue was neutralized with demineralized water and dried in a oven at 50 °C. TOC content was then measured on ~10 mg of homogenized residue using a CNS-analyzer (Fisons). Stable carbon isotope ratios were determined using an isotope ratio mass spectrometer (Finnigan Delta Plus) coupled online to the CNS analyzer. Absolute reproducibility, based on international and in-house standards, for TOC (Figure 2a) and $\delta^{13}C_{TOC}$ (Figure 2b) was better than 0.1% and 0.05‰, respectively. This data set is available from the Pangaea data repository (https://doi.org/10.1594/PANGAEA.884760) and was previously used for stratigraphic purposes (Frieling et al., 2018).

The $\delta^{13}C_{TOC}$ and TOC data allow for the generation of a basic age model based on published information on the duration of the CIE (e.g., Murphy et al., 2010; Röhl et al., 2007). Moreover, the recognition of orbital precession in lithological cycles in the Paleocene and Eocene sedimentary record at Site 959 (Cramwinckel et al., 2018), which are also expressed in, for example, trace elements and magnetic susceptibility (Frieling et al., 2018) provides additional constraints on sedimentation rates.

2.2.2. TEX_{86}

For TEX_{86} analysis, ~10 g of freeze-dried powdered sediment was extracted by a Dionex Accelerated Solvent Extractor 200 using dichloromethane (DCM):methanol (9:1 vol:vol) at 100 °C, 7×10^6 Pa. Extracts were separated into polar and apolar fractions over an Al_2O_3 column using methanol:DCM 1:1 and hexane:DCM 9:1 as respective eluents. To analyze glycerol dialkyl glycerol tetraethers (GDGTs), hexane:isopropanol 99:1 was added to the polar fraction, which were then filtered over a 0.45 μm PTFE filter and measured on an Agilent 1260 ultrahigh performance liquid chromatography mass spectrometer (UHPLCMS) at Utrecht University

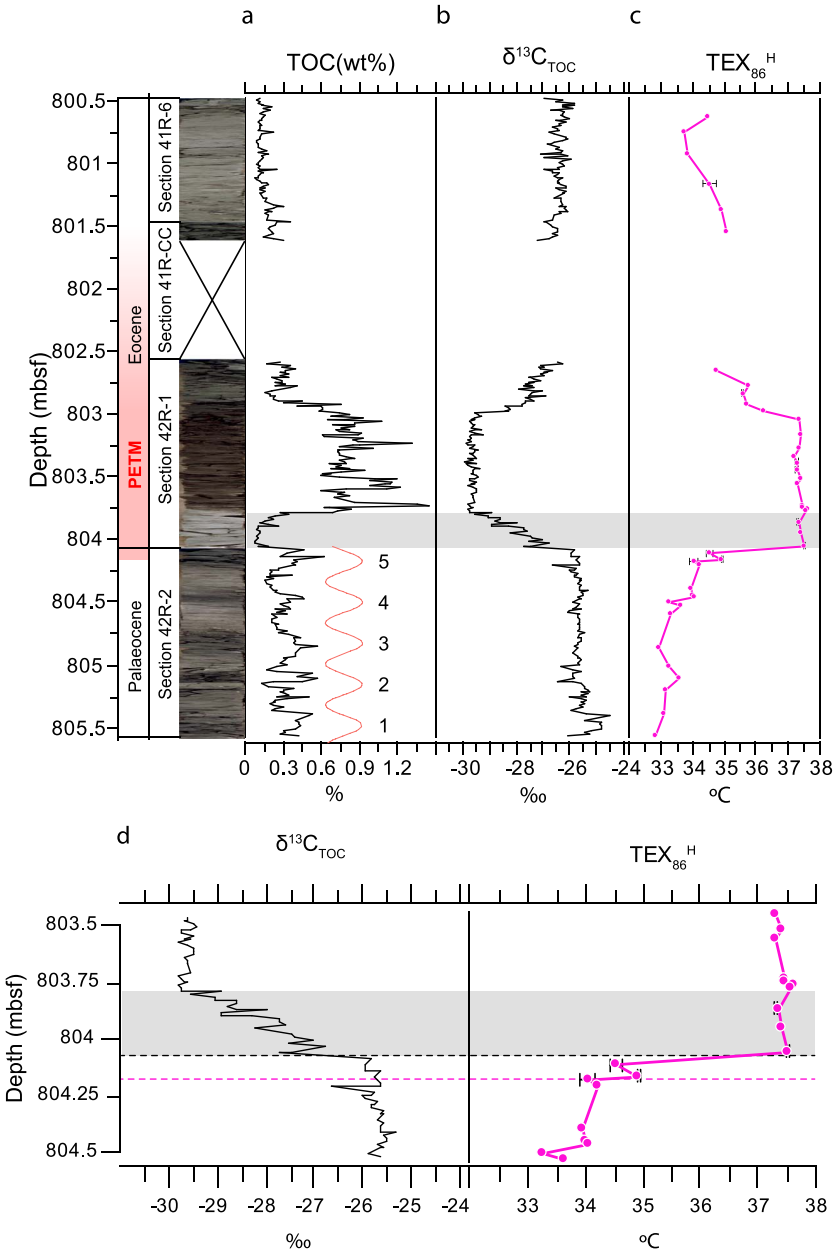

Figure 2. PETM at Ocean Drilling Program Site 959, Equatorial Atlantic. (a) TOC in weight percentage (TOC wt%) and 0.33 m filter from spectral analysis (red line). (b) Stable carbon isotope ratios of TOC ($\delta^{13}C_{TOC}$). (c) TEX_{86}^{H}-derived sea surface temperatures, error bars represent 1 sd derived from replicate analyses. Gray shaded band represents the turbiditic organic-lean layer. (d) Enlarged view of onset of the warming (pink dashed line) and carbon isotope excursion (black dashed line). Gray shaded band represents the turbiditic organic-lean layer. PETM = Paleocene-Eocene Thermal Maximum; TOC = total organic carbon; TEX = TetraEther indeX.

following standard methods (Hopmans et al., 2016). In addition to measuring in-house TEX_{86} and branched and isoprenoid tetraether index (BIT; Hopmans et al., 2004) standards, 9.9 ng of a C_{46} GDGT standard (*m/z* 744) was added to all samples to facilitate quantification of GDGTs. Fifteen samples were measured in duplicate to assess reproducibility. Reproducibility was always better than 0.01 TEX_{86} units and 0.005 BIT units, respectively, and reproducibility of in-house standards was always better than 0.01 and 0.03 for TEX_{86} and BIT. We use the BIT index and methane indices to assess influences of terrestrial (Hopmans et al., 2004; Weijers et al., 2006), methanotrophic (Zhang et al., 2011), and methanogenic (Weijers et al.,

2011) GDGT producers on TEX_{86} and did not find evidence for potential biases in any sample. The ring index (Zhang et al., 2016) indicates GDGT distributions are indistinguishable from the modern core-top calibration (Figure S1) and low GDGT2/3 ratios (<5) indicates deep water GDGTs likely do not contribute significantly to the GDGT pool (Sinninghe Damsté et al., 2012). The percentage of Red Sea type GDGTs (%Red Sea) is high, which is expected since %Red Sea GDGTs is also strongly influenced by temperature (Inglis et al., 2015). There are no indications that the setting at Site 959 was in any way analogous to the Red Sea. All raw data and indices values are included in Data Set S1.

Concentrations of GDGTs can be a limiting factor (Schouten et al., 2007) in organic lean sediments, such as encountered here at Site 959, and extremely low concentrations become more prevalent further down-core. We selected samples with >5 ng of UHPLCMS injected GDGTs, which amounts to approximately 1 ng/g sediment. GDGT concentrations per gram during the body of the CIE are ~50 times higher than outside the CIE, signaling enhanced preservation and/or (export) production of these lipids.

Several calibrations based on modern seafloor data exist to convert TEX_{86} values to SST. In this work, the absolute SSTs are of secondary importance to the timing of trends in the data set. We apply two of these calibrations, TEX_{86}^{H} (Kim et al., 2010) and BAYSPAR (Tierney & Tingley, 2014; Figure S1), but for clarity only show TEX_{86}^{H} in the main text and figures.

2.2.3. Inductively Coupled Plasma-Optimal Emission Spectroscopy and Barium Burial Rate Compilation

Bulk sediment geochemistry was determined for 50 samples across the CIE interval. Approximately 125 mg of freeze-dried sediment was powdered and then dissolved in 2.5 ml HF (40%) and 2.5 ml of $HClO_4/HNO_3$ mixture in a closed Teflon bomb at 90 °C overnight. The acids were then evaporated at 160 °C and the resulting gel was subsequently redissolved in 1 M HNO_3 at 90 °C during another night. Total elemental concentrations were determined by Inductively Coupled Plasma-Optimal Emission Spectroscopy (Perkin Elmer Optima 3000) at Utrecht University. Precision and accuracy was better than 5%, based on calibration to standard solutions and checked against internal laboratory standard sediments.

For the barium (Ba) burial compilation, we compile data from the deep ocean using the data set of Ma et al. (2014) as a starting point, and add new data and published values from literature. Non-detrital Ba or excess Ba (Ba_{excess}) concentrations are calculated from measured Ba concentration data (Reitz et al., 2004) using regional detrital Ba/Al ratios (e.g., 0.0045 determined for the Congo Fan; Rutsch et al., 1995) or global average detrital Ba/Al ratios (0.0037) if regional estimates are not available. The Ba data from each site are separated into latest Paleocene and PETM bins based on carbon isotope stratigraphy. Data points from strata directly below the CIE are designated as "latest Paleocene" and data from the body of the CIE is designated as "PETM."

2.2.4. Data Selection and Statistical Methodology

If the ^{13}C-depleted carbon that caused the CIE was the primary forcing of PETM warming, no time lag is expected between the two parameters since short feedbacks in the climate system operate on time scales (up to 10^2 years) much shorter than the time represented by our sampling intervals. To investigate if warming might have triggered ^{13}C-depleted carbon injection on millennial time scales, we apply ccfs on the temperature-$\delta^{13}C$ data to determine the optimal lead or lag across a 100 kyr period around the onset of the CIE. Each data set is resampled at 1 kyr resolution and shifted with 1 kyr increments. We assume the position of the maximum correlation coefficient (r^2) between temperature and $\delta^{13}C$ to be the most likely lead-lag relation. The data sets were also resampled at the resolution of $\delta^{13}C$ or temperature and subjected to the same analysis. This yielded similar results, implying that the interpolation did not affect the outcome of the analysis. In general, these analyses are similar to those performed in Zeebe et al. (2016), with the notable difference that a much longer interval is analyzed here, including periods in which $\delta^{13}C$ does not markedly change.

All r^2 values are highly significant because temperature and $\delta^{13}C$ records are very similar at all sites. However, since the data represent a variable mixture of rescaled and interpolated points, we cannot perform a meaningful Fisher r-to-z transformation on the correlation coefficients for each individual site to address significant differences between correlations. To further assess the robustness of our analyses and the influence of random scatter in the data, we conduct several sensitivity experiments. We subjected synthetic time series ($n = 100$) of $\delta^{13}C$ and SST without temporal offset to the same ccfs as the data sets.

The synthetic time series are designed to replicate the null-hypothesis that changes are synchronous and include a 4‰ and 4 °C shift from stable background to a stable plateau. We subsequently add random scatter of ±0.5‰/°C, ±1‰/1 °C, and ±2‰/2 °C. Perhaps with the exception of the Site 689 and 690 data (see also paragraph 3.3), which are based on replicate single-specimen planktic foraminifer analyses, the data are most similar to the lowest scatter scenario. The sensitivity analyses (Figure S2) show that false positive leads or lags (i.e., maximum correlation not at 0) may be found if the scatter is equal to or exceeds 1‰ and 1 °C. However, although 15 out of 100 analyses showed a lead or lag at a random ±1‰/1 °C perturbation, the false positives did not exceed 1 kyr in these synthetic data sets. We therefore argue the chance of one or multiple false positives in our data is very small.

We summarize the lead-lag data from individual sites by plotting kernel densities of the optimal correlations of each site and bootstrapped (n = 1,000) means of that data, with the note of caution that the amount of available sites and data still limits the ability to address true confidence intervals of the lead lag relations.

We correct the seawater $\delta^{18}O$ values for ice-free conditions (−1‰) and paleolatitude (−0.24‰; Zachos et al., 1994) and calculate temperatures following Kim and O'Neil (1997). For our calculations of temperature, we assume no changes in seawater $\delta^{18}O$ across the PETM. We also do not correct for any $\delta^{13}C$ or $\delta^{18}O$ changes as a result of pH decrease across the CIE (Penman et al., 2014), and therefore we potentially underestimate peak PETM temperatures by ~1 °C (Uchikawa & Zeebe, 2010). This has no influence on our lead-lag relations.

3. Results and Discussion

3.1. CIE and Site 959 Age Model

The $\delta^{13}C_{TOC}$ record at Site 959 shows a ~4 ‰ drop starting at 804.1 mbsf, stable low values from 803.8 to 803.0 mbsf, followed by a recovery to values slightly lower than those prior to the event (Figure 2c). We interpret this as a relatively complete PETM CIE section that includes the onset, body, and recovery of the CIE (Frieling et al., 2018).

3.1.1. The Onset of the CIE at Site 959

The shape of the onset of the CIE at Site 959 is somewhat anomalous, certainly for an open ocean site (Figure 2b), with a gradual decrease to PETM values and apparent scatter. The onset of the CIE marks the deposition of biosilceous muds/oozes which have been altered to porcellanite. The light appearance of this horizon, associated with very low TOC concentrations (Figure 2), stands out relative to surrounding strata. Since all biogenic silica has been altered to quartz or been replaced by pyrite, detailed micropaleontological analysis is not possible. A step in $\delta^{13}C_{TOC}$, TOC, and TEX_{86} may suggest a small discontinuity at the base of the porcellanite (804.09 mbsf) although this might also be a primary feature of the onset of the CIE.

Records of late Paleocene and early Eocene biogenic silica-rich deposits are relatively scarce and the ocean is generally assumed to be strongly undersaturated with respect to dissolved silica during this period (Siever, 1991). Furthermore, the position of the deposit, at the start of the period of warming poses another problem, since warming enhances the solubility of silica. This implies that biogenic silica deposition and burial must have been rapid to prevent dissolution. We note that enhanced silica preservation due to a potential additional supply of dissolved silica from increased weathering (Penman, 2016) was unlikely established immediately at the onset of the PETM. This suggests that (a) the biogenic silica was produced elsewhere and redeposited at the drill site by a mass-movement or (b) produced locally and deposited at a rate sufficient to inhibit immediate dissolution. If the biosilica layer represents a redeposition of material, similar concentrations of siliciclastic material compared to the late Paleocene imply that the silica likely did not derive from the African shelf. Rather, it is more likely derived from higher elevations on the marginal ridge and deposited through a mass-movement such as a turbidity current.

Turbiditic sequences in slope sediments are normally readily identified as fining upward Bouma-sequences. Although we find no obvious changes in grainsize, presumably because the supply of coarse siliciclastic material to this open ocean site is minor and foraminifera are absent in this layer. However, higher Ti/Al ratios (Figure S3; Frieling et al., 2018) at the base of the biogenic silica layer suggest heavy minerals are more concentrated there, a signal similar to Pleistocene Mediterranean turbidites (Wehausen & Brumsack, 1998). Turbidite deposits and slope failures are common in PETM shelf and slope deposits, where they are typically

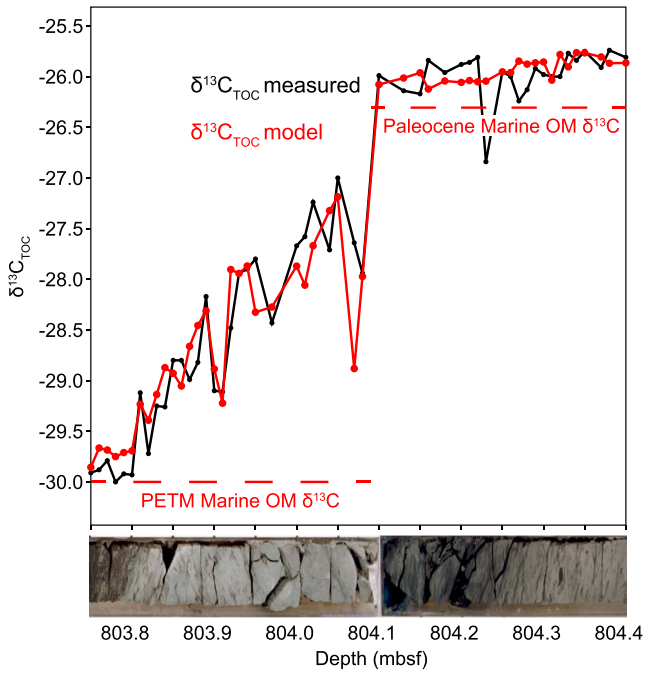

Figure 3. Organic carbon $\delta^{13}C$ record across the onset of the carbon isotope excursion and corresponding results of the mixing model. Core picture on bottom indicates an increasing contribution of dark-colored burrows toward the top of the white silica layer, consistent with increasing contributions of ^{13}C-depleted PETM organic matter. TOC = total organic carbon; PETM = Paleocene-Eocene Thermal Maximum.

interpreted to result from increasing sediment supply due to intensification of the hydrological cycle (Sluijs et al., 2014), but they may also be associated with submarine hydrate destabilization (Katz et al., 1999).

The amount of siliclastic material in the biogenic silica layer is not very different from that in underlying sediments, which implies the siliclastic material is not diluted by enhanced biogenic silica production. Therefore, if the biogenic silica is produced locally and preserved due to enhanced accumulation, a proportionally similar increase in supply of siliciclastic material must be invoked. Finally, to account for the apparent lack of organic matter, these effects have to be combined with more aggressive oxidation, which is unlikely in a warming environment with expanding oxygen minimum zones (Carmichael et al., 2017; Frieling et al., 2018; Sluijs et al., 2014; Zhou et al., 2016). Although local production and rapid accumulation cannot be completely excluded, a turbiditic origin for the biogenic silica at the onset of the PETM is the easiest explanation with the available evidence.

Regardless of the mechanism of deposition, rapid deposition of biogenic silica at the onset of the PETM provides an explanation for the anomalous shape of the CIE onset. The porcellanite yields very low TOC concentrations (Figure 2a), likely the result of extensive oxidation, leaving only a highly resistant fraction. Such resistant organic matter (OM) is typically clay-bound terrestrial OM (TOM), which in the Paleogene has a much higher $\delta^{13}C$ than marine OM (Sluijs & Dickens, 2012). Because the porcellanite is located at the onset of the CIE, it is likely that the resistant OM is of latest Paleocene age. If so, the low $\delta^{13}C_{TOC}$ values in this layer reflect a mixture of Paleocene OM with high $\delta^{13}C$ and PETM organic matter that is bioturbated down into the sediment. This is consistent with visual observations of the core material, which shows bioturbation of dark-colored PETM material down into the light porcellanite downcore (Figure 3).

3.1.2. Organic Matter Isotope Mixing Model

We test this hypothesis with a simple sediment mixing model, in which we assume that a small (0.03% TOC) but constant fraction of resistant Paleocene TOM with a $\delta^{13}C$ of −23‰, consistent with late Paleocene TOM (Sluijs & Dickens, 2012), is present in all samples. The BIT values and kerogen composition from the body of the PETM and late Paleocene indicate that the organic matter in these intervals is nearly exclusively marine. The PETM marine organic matter has $\delta^{13}C$ values of around −30‰ and latest Paleocene marine OM is assumed to be −26.3‰, which is consistent with published marine organic matter records (Sluijs & Dickens, 2012). We subsequently calculate $\delta^{13}C_{TOC}$ from measured TOC values (Figure 3) with the following isotope-mass balance equation:

$$\delta^{13}C_{TOC} = \left((TOM/TOC)^{*}\ \delta^{13}C_{TOM}\right) + \left(((TOC-TOM)/TOC)^{*}\ \delta^{13}C_{MOM}\right).$$

With the exception of one data point in the Paleocene and one during the gradual $\delta^{13}C$ decrease, this simple mixing model is capable of accurately matching both the drop from Paleocene to PETM values, as well as the smaller-scale variability in the measured $\delta^{13}C_{TOC}$ profile. We hence argue the gradual decrease in $\delta^{13}C_{TOC}$ is the result of bioturbation of overlying organic-rich sediments into the porcellanite. From these inferences it also follows that mixing from above influences reconstructed temperatures. GDGT concentrations during the body of the PETM are much higher than in the uppermost Paleocene and oxidation likely led to even lower initial GDGT concentrations in the porcellanite. Therefore, it requires only a fraction of PETM organic matter to completely overprint the original GDGT signal. Because of the extensive bioturbation and mixing, we exclude data from the porcellanite layer (804.1–803.8 mbsf) from further analyses.

3.1.3. Integrated Age Model

We use the published biostratigraphy and cyclicity in TOC wt% to construct a detailed age model for Site 959. The presence of *Rhomboaster bitrifida* in the core-catcher of Core 959D-41R (801.49–801.65 mbsf) is used as a

biostratigraphic proxy for *Campylosphaera eodela* and indicates nannoplankton Subzone CP8b. This sample is further marked by the highest occurrence of *Fasciculithus*, also indicating a latest Paleocene age (Shafik et al., 1998).

We identify a dominant periodicity of ~0.3 m in the interval from 805.6 to 804.1 mbsf using spectral analyses, where we find ~5 cycles observed in TOC wt% (Figure 1a). Following the biostratigraphic constraints these cycles occur on time scales of climatic precession (21 kyr), similar to cycles found throughout the Eocene (Cramwinckel et al., 2018) and in the Cretaceous (Beckmann et al., 2005) at this site. We hence attribute these TOC cycles to precession, implying compacted sedimentation rates of ~1.3 cm/kyr in the upper Paleocene, consistent with long-term sedimentation rates derived from biostratigraphic constraints (1–2 cm/kyr). If the anomalous biogenic silica layer indeed represents turbiditic deposition, the base of the current may have caused some scouring and thus there might be some sediment missing, although we have not noted a marked erosional surface or any other indication that sediment may be missing in this critical interval during sampling.

Calculated sedimentation rates during the body of the CIE (803.8–803 mbsf) are possibly somewhat lower if the body of ~70 (Röhl et al., 2007) or ~100 kyr (Farley & Eltgroth, 2003) is complete (0.8–1.15 cm/kyr). However, comparison to apparently more gradual recovery at other sites might imply that the small step (+1.1‰) at the start of the recovery represents a small discontinuity or condensed interval. We here assume sedimentation rates of 1 cm/kyr above 803.8 mbsf.

3.2. TEX_{86} SST Estimates

Upper Paleocene (805.6–804.2 mbsf) TEX_{86}^{H}-derived SSTs (Kim et al., 2010) show a warming trend and average 33.5 (95% confidence interval: 32.9–34.3) °C, which reflects long-term Paleocene-Eocene warming (Cramwinckel et al., 2018) as also recorded at high latitudes (Bijl et al., 2009) and in the deep ocean (e.g., Zachos et al., 2008). Visual comparison of both records does not show a clear relation between TEX_{86} with the phase of precession-scale cyclic variations recorded in TOC wt%, although we have insufficient data to perform proper statistical tests. SST rises stepwise by 1.2 °C at 804.19 mbsf relative to the latest Paleocene average (95% confidence interval: 0.9–1.6 °C). Importantly, this warming is outside 2σ from the Paleocene mean as well as the Paleocene trend and occurs 10 cm below the first observable change in $\delta^{13}C_{TOC}$.

A second step of 2.7 (2.4–2.9) °C occurs at 804.09 mbsf, corresponding to the onset of the CIE, to values of 37.4 (37.2–37.6) °C during the body of the PETM (Figure 2c). Consequently, we estimate a ΔSST of 3.9 °C (3.6–4.1 °C) across the onset of the PETM. This may represent a minimum estimate because TEX_{86} values within the PETM (0.96) approach the maximum value of 1, which calibrates to 38.6 °C with the applied logarithmic TEX_{86}^{H} calibration (Kim et al., 2010).

Nevertheless, TEX_{86}^{H} absolute temperatures are in good agreement with late Paleocene and PETM temperatures derived from Mg/Ca, $\delta^{18}O$, and TEX_{86}^{H} palaeothermometry in a nearby shelf section from Nigeria (Frieling et al., 2017). BAYSPAR-derived (Tierney & Tingley, 2014) absolute SST estimates (41.0 °C) and SST change (6.7 °C; Figure S1b), however, are excessively high compared to this nearby shelf record.

3.3. Quantifying Global Lead-Lag Relations

Similar pre-CIE warming has been observed at two sites along the New Jersey Shelf, Bass River and Wilson Lake (Sluijs et al., 2007), and in the Bighorn Basin, Wyoming (Secord et al., 2010). At ODP Site 690 in the Southern Ocean, surface warming also preceded the CIE (Thomas et al., 2002) and the same is recorded at nearby Site 689 (Zachos et al., 2007). Apart from the terrestrial section in the Bighorn Basin, all of these sites have well-resolved high-resolution chemostratigraphy and/or biostratigraphy, temperature, and $\delta^{13}C$ data across the onset of the PETM. We refined age models for Bass River, Wilson Lake, and Site 689, which are sites with sediment accumulation rates across the onset of the PETM sufficient to extract millennial scale leads and lags (Text S1) and resampled each data set at 1 kyr resolution. The resulting pairs of $\delta^{13}C$ and temperature data were subjected to ccfs to identify lead-lag relations, assuming a linear relation between temperature and $\delta^{13}C$ (Figure 4c). To estimate robustness of this analysis, we conducted sensitivity experiments where we apply ccfs to nonoffset synthetic time series perturbed with variable random scatter (section 2.2.4 and Figure S2). For Site 959 we conducted sensitivity experiments where we varied the amount of time covered by the biogenic silica layer between 2, 6, and 10 kyr. This assumption has virtually no

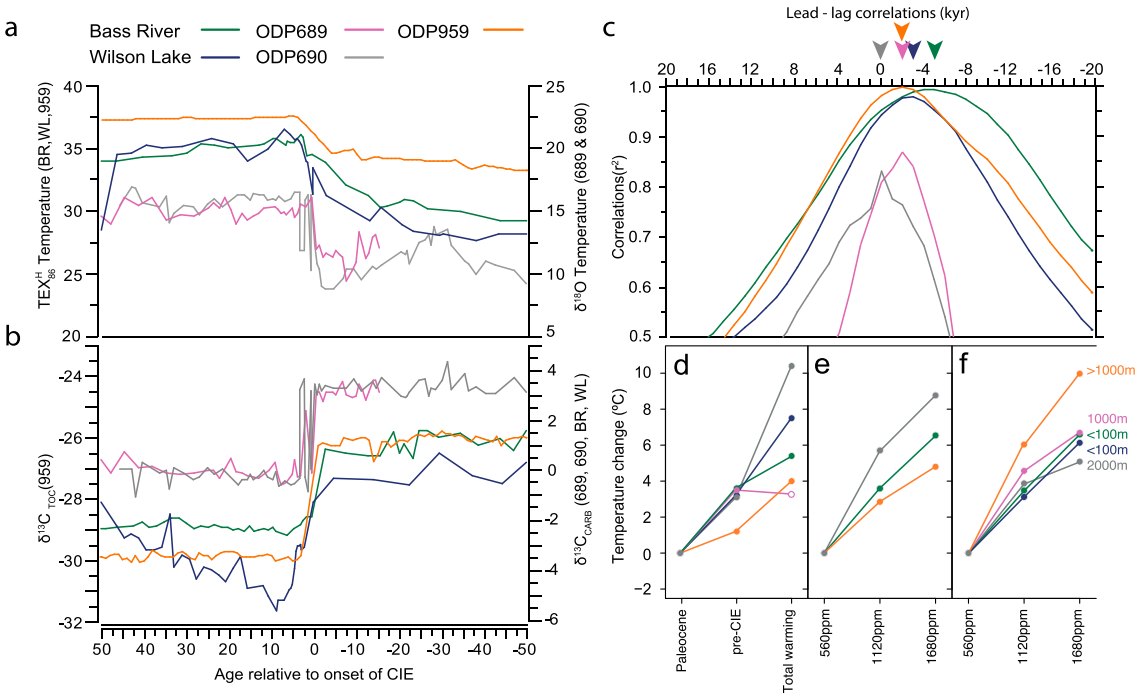

Figure 4. Cross-correlation functions of $\delta^{13}C$ and reconstructed temperature at all sites. (a) Sea surface temperature records from TEX_{86}^{H} (Bass River, Wilson Lake; both Sluijs et al., 2007, and ODP 959, this study; and $\delta^{18}O$; ODP 689, Zachos et al., 2007, and ODP 690, Thomas et al., 2002). (b) Stable carbon isotope records from bulk organic carbon (ODP 959), bulk carbonate (Bass River and Wilson Lake), and single specimen *Acarinina* (ODP 689 and ODP 690). (c) Correlation coefficients for each record relative to potential lead-lag relation in kyr. Arrows indicate position of highest value. (d) Observed sea surface temperature change as inferred from the data, separated into pre-CIE and full warming. (e) Modeled surface temperature change, differences between 1,120 and 560 ppm and difference between 1,680 and 560 ppm. Note that the pairs of ODP689/690 and Wilson Lake/Bass River are in the same grid cells and therefore have identical surface temperatures in the model. (f) Modeled bottom water temperature change and approximate water depth of each site at 56 Ma. ODP = Ocean Drilling Program; TEX = TetraEther indeX; CIE = carbon isotope excursion.

influence on further analyses, since values in both TEX_{86}^{H} and $\delta^{13}C_{TOC}$ remain almost unchanged during the entire body phase. The scenario with a 2-kyr hiatus is used for further analyses and Figure 4. Regardless of the assumptions used, the position of the maximum correlation is robust with respect to data quality and correlation window length.

All surface records, except the single-specimen *Acarinina* record at Site 690, show the highest degree of correlation when temperature leads the onset of the CIE (Figure 4c). These records are stratigraphically complex because of sediment mixing due to bioturbation effects (e.g., Kirtland Turner et al., 2017; Stoll, 2005) or perhaps slumping (Pearson, 2017). This makes lead-lag relations at Sites 689 and 690 less straightforward since the averaged carbon and oxygen isotope records used in the ccfs derive from a relatively limited number of replicate measurements of single specimen planktic foraminifera (Thomas et al., 2002). In such data sets mixing is potentially detrimental to the reliability of ccf results. Specifically, mixing has introduced an additional alternation between latest Paleocene (high $\delta^{18}O$ and high $\delta^{13}C$) and peak PETM (low $\delta^{18}O$ and low $\delta^{13}C$) values at Site 690. This alternation inevitably shifts ccf results to a lead-lag relation of zero, which is reflected in the Site 690 *Acarinina* ccfs distribution, which spikes at 0 (Figure 4c), while other sites follow a normal distribution. If this alternation is omitted, the optimal correlation shifts to a temperature lead of ~1 kyr at Site 690 (Figure S4), consistent with the *Acarinina* record from Site 689, which does not include a similar alternation.

Moreover, specimens with high $\delta^{13}C$ (pre-CIE) and low $\delta^{18}O$ (indicating warm conditions) values are present in both *Acarinina* and *Subottina* records from Site 689 and 690, providing strong evidence for pre-CIE warming (Figures S5 and S6). This is important for two reasons. First, unlike TEX_{86}^{H} records, the same substrates are measured for both $\delta^{13}C$ and temperature ($\delta^{18}O$), which excludes possible differential bioturbation between carbonates and organic matter. Second, although bioturbation effects and sedimentation

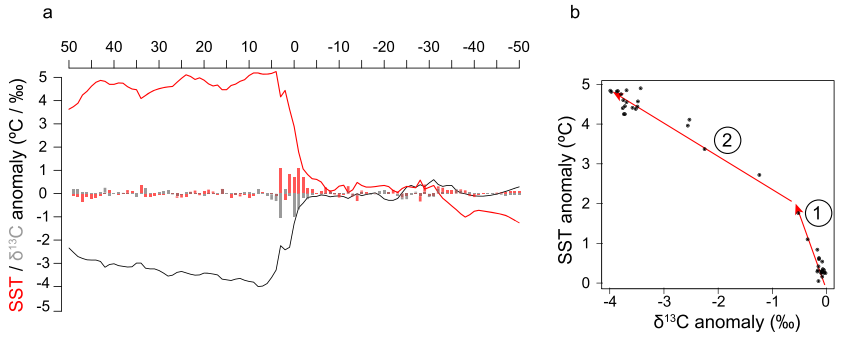

Figure 5. Average (Sites 689, 690, 959, Wilson Lake, and Bass River) SST and $\delta^{13}C$ anomalies from background Paleocene. (a) Lines represent averaged SST and $\delta^{13}C$ anomalies across the CIE (−50 to +50 kyr). Colored bars represent rate of change (°C and ‰ kyr^{-1}) in corresponding 1 kyr bins. (b) Cross plot of SST and $\delta^{13}C$ change close to the onset (−20 to +20 kyr), showing the transition from (1) warming under low rate of $\delta^{13}C$ change prior to the CIE and (2) warming under high rate of $\delta^{13}C$ change from the onset to peak CIE. SST = sea surface temperature; CIE = carbon isotope excursion.

rates are variable, the observed lead-lag relation between the onset of warming and the onset of the CIE is similar in sign and duration for all pairs of TEX_{86}^{H} and $\delta^{13}C_{carb}$ and $\delta^{13}C_{TOC}$ records (Figure 4c), implying a stratigraphic displacement bias between different signal carriers in our data sets is unlikely.

Using the optimal correlations for each site, we estimate the spread of the mean using a bootstrap approach. On average, temperature leads the CIE by 2 kyr (95% quantiles 3.6–0.8 kyr lead). Importantly, temperature rose by ~2 °C directly prior to the CIE, and ~3 °C simultaneously with the onset of the CIE (Figures 5a and 5b).

3.4. Temperature Proxy-Data Climate Model Comparison

Collectively, we find that records from northern midlatitudes, the tropics, and the Southern Ocean show that sea surface warming led the CIE. Even though no records from the Indo-Pacific sectors with sufficient resolution are available, this indicates that this warming was most likely global in nature. To further substantiate this and explore how these changes translate to deeper water, we compare to a fully coupled Atmosphere Ocean General Circulation Model (HadCM3L; Hadley Center Coupled Model version 3), running at low ocean resolution, configured with early Eocene paleogeography, and with 560, 1,120, and 1,680 ppm (2, 4, and 6 times preindustrial) CO_2 in the atmosphere (see Lunt et al., 2010, for detailed model run description). The early Eocene climate sensitivity (global mean temperature change under a doubling of atmospheric CO_2 concentrations) in this model is 3.6 °C. Regional changes in the degree of warming from the 2 to 4 and 6× preindustrial scenarios occur due to oceanographic changes (Lunt et al., 2010), similar to results in the CESM1 model (Frieling et al., 2017). Although our coverage is limited to the Atlantic, the temperature response in the sampled regions of the Atlantic is similar to the zonally averaged response in (paleo)climate models (e.g., Frieling et al., 2017; Lunt et al., 2012). We also find good agreement between the magnitude of pre-CIE and total warming from the study sites and a doubling and tripling of CO_2, respectively (Figures 4d and 4e), implying that the spatial variability of pre-CIE warming is consistent with global warming.

The magnitude of pre-CIE surface warming (~2 °C) is similar to variability in Paleocene deep ocean temperature (Littler et al., 2014). However, deep ocean temperatures reflect high latitude (winter) temperatures and the persistence of polar amplification in these extremely warm climates (Frieling et al., 2017) implies that pre-CIE warming in deep waters was larger than the global average surface temperature change. More importantly, the rate of pre-CIE warming (~2 °C in less than 10 kyr) was higher than background Paleocene temperature variability on orbital time scales (maximum 0.2‰ or ~0.8 °C at climatic precession scale, see, e.g., Littler et al., 2014).

3.5. PETM Related Ba Cycle Perturbations

Many localities in the open ocean show elevated excess Ba accumulation during the PETM (e.g., Bains et al., 2000; Ma et al., 2014). This observation has previously been linked to two different mechanisms with fundamentally different consequences for the interpretation in terms of the carbon cycle (Dickens et al., 2003; Ma et al., 2014). First, elevated Ba burial was postulated to signify elevated export productivity (Bains et al., 2000;

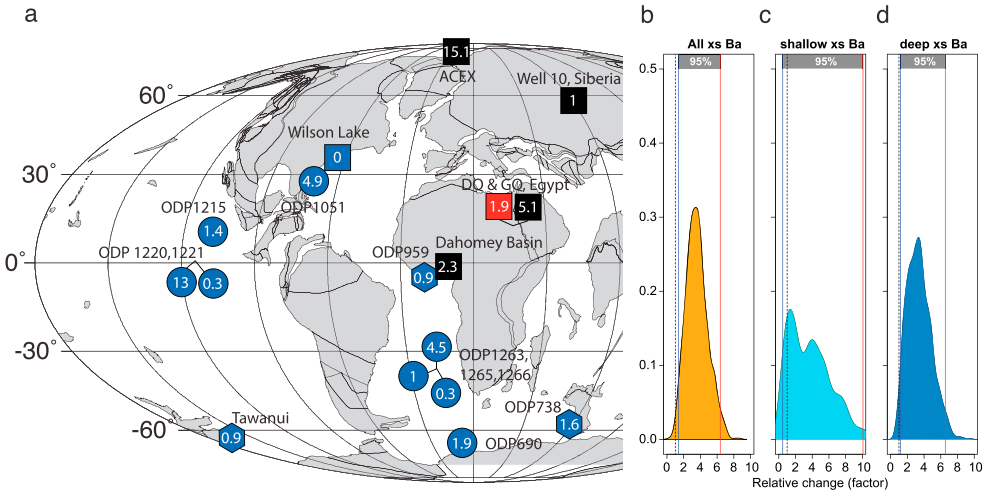

Figure 6. Global compilation of barium burial rate change. (a) Numbers in circles represent relative change at each site: A factor of 1 indicates no change. Symbol type indicates setting: circles = deep ocean; hexagons = slope; squares = shelf and epicontinental seaway. Color coding indicates oxygenation during the CIE: blue = oxic-dysoxic; red = anoxic; black = evidence for euxinic conditions. Site abbreviations—DQ = Dababiya Quarry; GQ = Gabal al Qreiya. Data sources for Ba and oxygenation regime can be found in Table S1. (b) Density of bootstrapped means of excess (xs) Ba. (c) Density of bootstrapped means of excess Ba at shallow sites. (d) Density of bootstrapped means of excess Ba at deep sites. Dashed line in panels (b)–(d) indicates no change (factor = 1). Note that a detrital correction was not possible for Site 738C and DQ and therefore these sites have not been used for the analyses in panels (b)–(d). ODP = Ocean Drilling Program.

Ma et al., 2014), based on only open ocean records. Because Ba has an oceanic residence time less than 10 kyr, which is much shorter than the time scales of the PETM, this was interpreted as a shift in Ba burial from the shelf seas to the open ocean (Paytan et al., 2007). Such a shift would have been facilitated by regeneration of Ba on the shelf, because of widespread anoxia (e.g., Dickson et al., 2012). Second, potentially in conjunction with the first mechanism, Dickens et al. (2003) used a simple box-model to show that destabilization of 2000 Gt of methane hydrate could result in a large transient (twofold) increase in global Ba accumulation rates. These two hypotheses yield very different implications: While elevated export productivity could represent a negative carbon cycle feedback (Ma et al., 2014), because of the associated enhanced carbon storage, the release of methane hydrates represents a strong positive carbon cycle-climate feedback (Dickens et al., 1997).

Here we compile Ba burial rates from the latest Paleocene and the CIE from the available large suite of sites from shelf to deep settings (Figure 6). We build on the previously published deep ocean compilation of Ma et al. (2014) and add new data from Site 959 (Data Set S1), two sites in Egypt, Southern Tethys (Soliman, 2003; Soliman et al., 2011), the Well 10 Section in the West Siberian Sea (Data Set S1), Wilson Lake, New Jersey Shelf (Quattlebaum, 2004), Lomonosov Ridge, Arctic Ocean (März et al., 2010), Dahomey Basin, Nigeria (Data Set S1), Tawanui, New Zealand (Crouch, 2001), and ODP Site 738 (Yasukawa et al., 2017). These data are correlated using the CIE and distinctive phases within the CIE such as onset, body, and recovery. Subsequently, data prior to the CIE are labeled as latest Paleocene and data from the body of the CIE are considered PETM. Although this approach does not guarantee consistent sampling between sites through time, the number of data points is sufficient to compare the late Paleocene to the PETM.

First, we have separated the data sets for which excess Ba fluxes have been determined (Figure 6b). Subsequently, we separated continental margin locations (Figure 6c) from deep-sea sites (Figure 6d). As expected, there is substantial heterogeneity in the excess Ba flux change at marginal sites. Importantly, however, our compiled data show that the majority of these sites show an increase in excess Ba burial and that the increases are generally much more extreme than the Ba burial reductions at other sites. This is expressed by the median growth factor, which is 3.7 (factor 0.5 to 10.1 within the 95% confidence interval; Figure 6c). The probability that the value is equal to or smaller than 1 is approximately 17%, so this possibility cannot be excluded. An increase in Ba burial is however much more likely. In fact, the probability is 68% for a value of 2

or larger. The only marginal marine site that shows significant loss of biogenic Ba during the PETM is Wilson Lake (New Jersey), which has low Ba concentrations throughout. Site 959 and Tawanui (New Zealand) show a minor decrease in excess Ba burial (factor 0.9). It is therefore likely that biogenic burial rates rose along continental margins.

We note that even though our compilation covers a large range of settings and environmental conditions, it suffers from uncertainties in accumulation rate estimates and therefore might not fully capture the global heterogeneity in Ba accumulation. It should also be noted that barite may have been remobilized in some of these sediments and precipitated secondarily. Although we cannot fully exclude that our results are influenced by such a sampling bias, the relatively large number of sites should at least partly address the issue of spatial heterogeneity and age model uncertainties. Indeed, although we cannot completely exclude an influence of widespread seafloor deoxygenation and subsequent regeneration and reprecipitation of Ba, it has no obvious influence on intersite variability in Ba burial or %excess Ba in the present data compilation across the PETM. Because excess Ba burial also rose in the deep sea (Figure 6c), the currently available data support a global average increase, certainly in the deep sea and most likely along continental margins. We find this is an important observation as in the modern system Ba burial in the deep ocean clearly dominates over burial on the shelf (Dymond et al., 1992).

This implies that our compilation of shelf and mid-depth sites shows no evidence for a switch from high to low accumulation rates of biogenic Ba from the Paleocene to the PETM due to development of anoxic bottom waters. No systematic differences in excess Ba burial rate changes are observed related to location, oxygenation, or productivity regime, even though our compilation covers a large range of environmental conditions, including sites where anoxic bottom waters developed during the PETM (Figure 6 and Table S1). Overall, excess Ba burial increases by a factor ~3.5, and while significant uncertainty remains about the magnitude of increase (95% confidence interval 1.4 to 6.6), the probability of a decrease is <1% (Figure 6b). Collectively, based on the present set of Ba burial data, we conclude that global average Ba burial rates during the PETM increased with respect to the late Paleocene.

Although previous authors have suggested that a Ba peak may coincide with the onset of the CIE (Ma et al., 2014), none of the existing Ba and $\delta^{13}C$ records allow for detailed lead-lag analyses we performed for $\delta^{13}C$-SST pairs. Therefore, the exact temporal relation of the Ba increase to the CIE remains elusive. Indeed, compared to the $\delta^{13}C$-SST relation, the relation between $\delta^{13}C$ and Ba may be even more complicated, because multiple carbon sources are in play (Frieling et al., 2016; Panchuk et al., 2008; Zeebe et al., 2009) and these sources may or may not affect the Ba cycle. We can, however, confidently compare background Ba burial to Ba burial during the CIE. From this, we surmise that long-term (>10 kyr) average Ba burial rates increased during the PETM. This implies that, unless a currently unresolved complex combination of reprecipitation and regeneration of Ba from anoxic sediments or a sampling bias plays a role, additional Ba input is required to balance excess burial at this spatial and temporal scale.

3.6. Potential Causes for Increased Global Marine Ba Fluxes

While a rise in global Ba burial rates both during the PETM along continental margins and in deep sea settings emerges from the data compilation (Figure 6), identifying the source(s) is(are) more complex. Here we consider two potential sources for additional input of dissolved Ba: enhanced weathering and methane hydrate-related inputs.

First, an increase in continental weathering (Ravizza et al., 2001) and enhanced sediment discharge from land to ocean (e.g., Hollis et al., 2005; Kopp et al., 2009; Sluijs et al., 2014) might have contributed to the increased supply of Ba during the PETM. However, an increase by a factor of ~3 seems unrealistic and not in line with the observed increase being more or less simultaneous with the onset of the CIE. Weathering inevitably would need time to effectively alter the input, resulting in a considerable time lag. Most importantly, this would also increase overall terrigenous Ba, which is not observed to the same degree as biogenic barium increases.

Second, destabilization of marine methane hydrates and an associated release of pore water rich in dissolved Ba and depleted in SO_4^{2-} may explain a large and sudden increase in Ba supply on shorter time scales (Dickens et al., 2003). Dickens et al. (2003) calculated that a release of 2,000 Gt of methane hydrates could account for a doubling in Ba burial. However, Paytan et al. (2007) noted that releasing such large

amounts of dissolved Ba would rapidly supersaturate waters and hence result in mostly local barite precipitation. This would prevent the Ba released to advect to more open ocean settings, away from the shelf/slope settings, which is not in line with our observations (Figure 6).

It is possible that widespread shelf/slope anoxia (Dickson et al., 2012; Sluijs et al., 2014) prevented local burial of this excess barite, but we do not observe a large dependency of Ba burial to seawater oxygen content in our compilation (Figure 6). However, how localized Ba would precipitate also depends on sulfate concentration. Although direct evidence is lacking, Algeo et al. (2015) and Lowenstein et al. (2001) indicated that early Cenozoic seawater was likely comparatively low in sulfate. Much lower (10–15 mM compared to modern, 28 mM) sulfate concentrations in the early Paleogene (see also Kurtz et al., 2003) might allow more Ba to build up in seawater and travel further from its source. Still, it remains unclear how these factors affected Ba distribution, saturation, and burial on these time scales pending suitable modeling.

Paytan et al. (2007) also argued that increased Ba concentrations should be reflected in lower Sr/Ba ratios in barite. Accordingly, Sr/Ba of barite (Paytan et al., 2007) and Ba/Ca of foraminifera do not show a marked change across the PETM. This implies that the saturation state of $BaSO_4$ in seawater likely did not appreciably vary across the PETM. Hence, although the flux of $BaSO_4$ to the sediment increased (Figure 6), a steady state must have been maintained. This is in line with foraminifera Ba/Ca ratios showing stable dissolved Ba^{2+} across the PETM (Hall et al., 2004). In the open ocean, precipitation and sedimentation mechanisms were likely similar to today and barite precipitation would be expected to be governed by organic matter remineralization processes (Dehairs et al., 1992). The distribution of Ba burial during the PETM was hence still modulated by local differences in export productivity (Ma et al., 2014) and perhaps temperature (John et al., 2013). Hence, a Ba release from dissociating methane hydrates does not preclude an export productivity related (re)distribution as previously suggested (Ma et al., 2014). However, the global increase in Ba burial fluxes by a factor of ~3 does require a large additional source of Ba and, despite the above outstanding issues, we argue massive methane hydrate destabilization is currently the only plausible candidate.

3.7. Methane Hydrate Presence and Dissociation

At intermediate depths (1–1.5 km) in the Atlantic (Figure 4f), the HadCM3L model results show enhanced warming (~6 °C per doubling of CO_2). Although this result may be model-dependent, it is a crucial observation, since methane hydrates were most likely to exist below ~900 m water depth in the Paleocene (Dickens, 2001b).

If methane hydrates destabilize, two main pathways can lead to rapid release of gaseous methane from marine sediments. First, if the bubble volume of methane in sediment exceeds a certain threshold value, these bubbles may reach the sediment-water interface, dissolve and oxidize to CO_2 (Archer & Buffett, 2005; Valentine et al., 2001). Although this can happen on small scales (cm-m), this scenario has also been connected to large (km) scale pockmarks, which have been found associated with Paleocene-Eocene sediments (Imbert & Ho, 2012). However, the exact age of these structures remains uncertain and the gas volume accounted for is equivalent to only ~1% of the total volume required to explain the CIE. The second way of releasing methane is more violent. The continental slopes, where hydrate-rich sediments typically occur (Kvenvolden, 2002), are also susceptible to sediment destabilization. Large masses of methane may have been released during the PETM more or less instantaneously from failure of the North American Atlantic slope based on seismic data (Katz et al., 1999, 2001). Interestingly, the turbiditic deposit at the onset of the CIE at Site 959 may suggest similar slope instability, perhaps caused by gas hydrate destabilization.

Crucially, carbon addition from methane hydrates is also a plausible mechanism to explain the observed regional patterns in CCD rise (Zeebe et al., 2009) and possibly deep water deoxygenation (Pälike et al., 2014), which cannot be easily achieved by oxidation of terrestrial organic matter in the atmosphere. Furthermore, pre-CIE warming at many locations (Figure 4d) was similar in magnitude as the hypothesized warming needed for large-scale methane hydrate dissociation (3–4 °C; Archer et al., 2009), which translates well to intermediate and bottom waters (Figures 4d–4f; Lunt et al., 2010). With the presently available data, the combination of early warming, globally elevated Ba burial rates, and the pattern of CCD changes and deoxygenation is only fully consistent with massive methane hydrate dissociation.

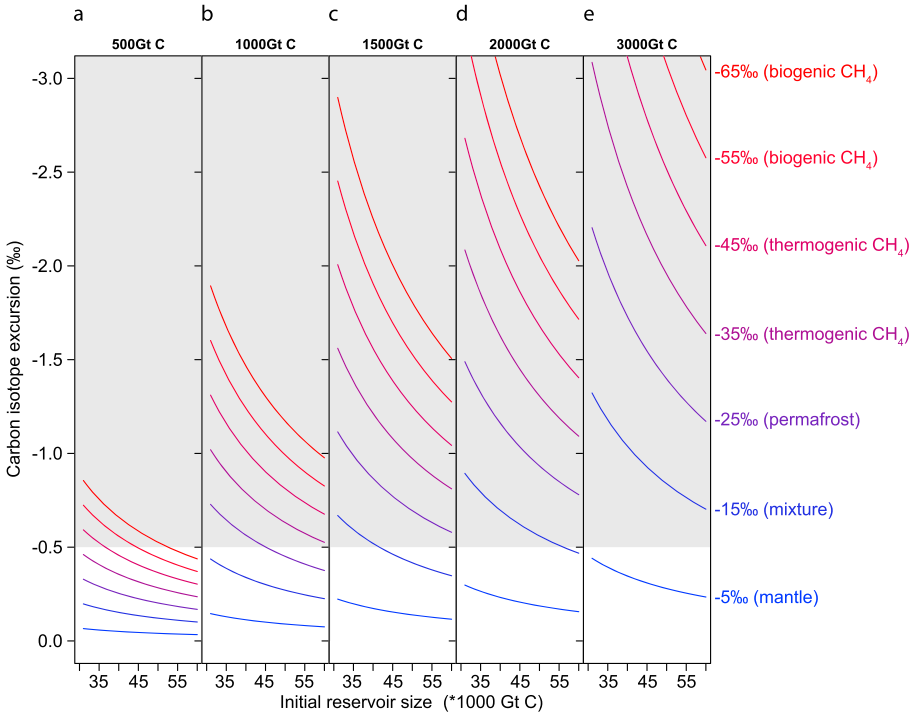

Figure 7. Mass balance equations across a $\delta^{13}C$ signature range of 5–65‰ and exogenic carbon pool size range of 35–55,000 Gt C, with variable input size. (a) 500 Gt C, (b) 1,000 Gt C input, (c) 1,500 Gt C input, (d) 2,000 Gt C input, (e) 3,000 Gt C input. The shaded area is considered detectable as a carbon isotope excursion (>0.5‰).

4. Scenarios for Early Warming

Discussion on potential carbon sources to explain the CIE, ocean acidification and warming started with the work of Dickens et al., who explored the methane hydrate theory (Dickens et al., 1995, 1997) as well as other potential sources (Dickens, 2001a). Subsequent work has delivered many interesting hypotheses, including marine and terrestrial organic matter sources, thermogenic methane, volcanism, lithospheric gas explosions, and bolide impacts (DeConto et al., 2012; Gutjahr et al., 2017; Kent et al., 2003; Kurtz et al., 2003; Morgan et al., 2004; Nisbet et al., 2009; Sexton et al., 2011; Svensen et al., 2004), as well as multiple sources (Frieling et al., 2016; Panchuk et al., 2008; Sluijs et al., 2007). We evaluate plausible sources of carbon explaining global warming prior to the onset of the CIE (Figure 4) using the same basic isotopic mass balance principles as Dickens (2001a) and basic considerations as laid out by several authors (e.g., Kump & Arthur, 1999).

Pre-CIE warming requires a source that has a $\delta^{13}C$ value similar to that of the ocean (i.e., close enough to 0‰ to limit the effect on sedimentary $\delta^{13}C$ records) and produces sufficient amounts of CO_2 on millennial time scales to cause 2 °C of surface warming. Below, we assess if biogenic and thermogenic methane, mantle CO_2, and terrestrial organic matter, notably thawing permafrost represent plausible sources by calculating their impact on global $\delta^{13}C$. While temperature cannot be estimated using simple equations, we emphasize that background CO_2 was likely high (Gehler et al., 2016), implying a very large C input is needed for a significant SST rise. Several modeling exercises independently arrive at 7,000 Gt C for the entire event (Meissner et al., 2014; Panchuk et al., 2008), mostly because climate models need excessively high CO_2 concentrations to reproduce the extremely high SSTs (e.g., Frieling et al., 2017). We therefore assume at least ~2,000 Gt C is needed for the observed 2 °C SST rise, given the commonly accepted range of equilibrium climate sensitivity (1.5–4.5 °C per doubling; IPCC, 2014; PALAEOSENS, 2012). For simple mass-balance calculations, we use a late Paleocene background exogenic carbon reservoir of 35,000 to 55,000 Gt C (Dickens, 2001a; Zeebe et al., 2009) and illustrate how variable $\delta^{13}C$ and input sizes affect the global exogenic carbon cycle (Figure 7):

Size of reservoir / (Size of input + initial reservoir * $\delta^{13}C$ of input).

Table 1
CO_2 Emission Rate Estimates From Enhanced Volcanism in the North Atlantic

Estimated magma production rate ($km^3 \cdot km^{-1} \cdot kyr^{-1}$)	Duration of activity "burst" (kyr)	Total length of rift (km)	Total magma volume (km^3)	Gt C (0.5 wt%CO_2)	Gt C (0.2 wt% CO_2)	Maximum Gt/year (0.5%)	Maximum Gt/year (0.2%)
2	20	2,560	102,400	384	154	0.019	0.008
2	10	2,560	51,200	192	77	0.019	0.008
2	5	2,560	25,600	96	38	0.019	0.008
3	20	2,560	153,600	576	230	0.029	0.012
3	10	2,560	76,800	288	115	0.029	0.012
3	5	2,560	38,400	144	58	0.029	0.012
6	20	2,560	307,200	1,152	461	0.058	0.023
6	10	2,560	153,600	576	230	0.058	0.023
6	5	2,560	76,800	288	115	0.058	0.023

4.1. Biogenic and Thermogenic Methane

It was recently shown that one thermogenic vent system was active during the body of the CIE (Frieling et al., 2016) and a seismic reflector corresponding to the top of this vent suggests this level correlates with activity of hundreds of such systems (Svensen et al., 2004). However, any thermogenic methane contribution prior to the main CIE must be relatively minor (maximum ~500–750 Gt C, depending on $\delta^{13}C$ range -30 to -45). On this basis, a significant release of biogenic methane as cause of pre-CIE warming is also excluded. Biogenic methane is even more ^{13}C-depleted (-50 to -70‰) and any biogenic methane input larger than 500 Gt C would already produce a larger negative CIE than observed (>0.5‰; Figure 7).

4.2. Volcanic Carbon From the North Atlantic Igneous Province

The evidence of enhanced volcanism in the North Atlantic is ample for the Paleocene, early Eocene, and close to the PETM (e.g., Eldholm & Thomas, 1993; Storey et al., 2007) and during the PETM (Frieling et al., 2016). A limiting factor in invoking a volcanic source, however, for early warming is the rate at which mantle-derived CO_2 can be injected to explain 2 °C of global warming within a few to tens of millennia (e.g., Dickens, 2001a). We calculate how much carbon could be produced from excess magma production within a short (5, 10, or 20 kyr) period (Table 1). The calculations assume the following constants; magma density is 2,750 kg/m^3 of which 0.2% to 0.5% (by weight) is CO_2, which is degassed completely (Self et al., 2006). The length of the active zone is 2,560 km (Eldholm & Grue, 1994). The magma production rates are taken from Storey et al. (2007) and recalculated to rates per kyr. The total volume of the flood basalts in the North Atlantic is ~1.8×10^6 km^3 (Eldholm & Grue, 1994), maximum and minimum volumes in our calculations are 3.1×10^5 km^3 (20 kyr, 6 $km^3 \cdot km^{-1} \cdot kyr^{-1}$, 2,560 km rift) and 2.6×10^4 km^3 (5 kyr, 2 $km^3 \cdot km^{-1} \cdot kyr^{-1}$, 2,560 km rift), respectively. It should be noted that the North Atlantic Igneous Province (NAIP) is emplaced in two main phases each spanning several Myr (e.g., Wilkinson et al., 2016) and that our rates are thus much higher than average, consistent with Storey et al. (2007). The modern volcanic C flux to the atmosphere is ~0.1 Gt/year (IPCC, 2014). These scenarios thus require an increase of volcanic CO_2 production, with respect to the global modern flux, of at least 10–60%. The volumes of C produced in our highest emission scenario therefore remain relatively small (~1,150 Gt C over 20 kyr) compared to the volumes typically used in carbon cycle modeling exercises (e.g., Gutjahr et al., 2017; Meissner et al., 2014; Panchuk et al., 2008; Zeebe et al., 2009).

One of the uncertainties in our calculations concerns the degassing parameter. Regardless of the CO_2 content of the magma, it is highly unlikely that all of that CO_2 was degassed, perhaps even more unlikely when the emplacement time of the flood basalts is rapid. However, all CO_2-content estimates are based on historical eruptions, which may or may not be representative for emplacement of a large igneous province. Given these uncertainties, we argue that the emission scenarios here presented are likely upper estimates and only used to illustrate plausibility. These scenarios clearly illustrate that longer (>10 kyr) periods of sustained enhanced activity are required and although it is impossible to connect the earliest warming to the volcanism with the presently available data, we note that first signs of warming are typically observed ~10 kyr before the CIE (Figures 4a and 4b). Intriguingly, a small decrease in Os isotopes, signaling increased

mantle-input, is observed directly prior to the CIE in and around the North Atlantic (Dickson et al., 2015; Schmitz et al., 2004; Wieczorek et al., 2013). However, this Os-isotope decrease is not comparable in magnitude to the decrease observed during activity from other large igneous provinces (e.g., Turgeon & Creaser, 2008). This is further supported by recent high-resolution mercury concentration data (Jones et al., 2019), which indicates an increase in volcanic activity prior to the CIE, but this increase is not of comparable magnitude as other periods of large igneous province emplacement. Although better dating and volumetric assessment of volcanic activity on <100 kyr time scales in the NAIP are needed to draw further conclusions, we find a modest volcanic CO_2 contribution to early warming is likely.

4.3. Orbital Trigger: A Role for Permafrost Thawing?

One problem with the volcanic-trigger scenario might be a component of orbital pacing of early Eocene negative CIEs, which correspond to maxima in 400 and 100 kyr eccentricity (Cramer et al., 2003; Lauretano et al., 2015; Littler et al., 2014; Lourens et al., 2005; Westerhold & Röhl, 2009). This would exclude a volcanic or any other catastrophic trigger. However, contrary to earlier findings the more recent studies indicate that the onset of the PETM did not occur during a maximum in 400 kyr eccentricity (Littler et al., 2014; Westerhold et al., 2017). Correspondence with the 100 kyr cycle is still possible. DeConto et al. (2012) suggested up to 3,700 Gt of C could potentially have been released from thawing Antarctic permafrost under favorable orbital configurations, particularly obliquity, to explain the entire event, including the CIE. However, no evidence exists for permafrost on Antarctica during the late Paleocene nor for its thawing or oxidation during the PETM. Moreover, apart from the Contessa section in Italy (DeConto et al., 2012), no power is apparent in the obliquity band in time series reflecting late Paleocene-early Eocene climate or carbon cycling. Based on mass balance calculations, a relatively modest release from this source (maximum ~1,100 Gt C, $\delta^{13}C$ approximately −23‰; Sluijs & Dickens, 2012) may be consistent with a $\delta^{13}C$ drop of ~0.5‰ (as observed here, see also Figure 5b) before the main CIE. Therefore, if true, this scenario should be accompanied by a global $\delta^{13}C$ decrease prior to the main CIE, which at this point may be beyond the limits of uncertainty.

Collectively, the lead-lag relation we identify and volumetric calculations based on currently available literature make a single dominant forcing for the entire PETM CIE, such as mantle-derived CO_2, as recently suggested (Gutjahr et al., 2017) or the impact of an extraterrestrial body (Kent et al., 2003) unlikely. It strongly suggests a scenario of positive feedbacks. We show that pre-CIE warming was global in nature and that, in principle, is inconsistent with orbital forcing. We therefore surmise that elevated volcanic activity pushed the hydrate system beyond the threshold for dissociation, leading to an extremely effective positive feedback. This is also consistent with the increase in Ba burial on a global scale we record.

5. Conclusions

We identify the Paleocene-Eocene boundary in ODP Site 959 in the eastern equatorial Atlantic. The PETM at this site is marked by a ~3.7‰ negative CIE in bulk organic carbon and ~3.9 °C of surface warming based on TEX_{86}^{H}. Crucially, the start of warming precedes the onset of the CIE. Based on statistical analyses of five high-resolution temperature-$\delta^{13}C$ data sets, we calculate that ~2 °C of global warming preceded the PETM CIE by ~2 kyr. This implies that a little more than half of the warming (~3 °C) and almost the entire (>80%) 3–5‰ global negative CIE may result from a positive carbon cycle feedback.

An assessment of global Ba burial rate, based on a data compilation, suggests that the average oceanic Ba burial rate rose by a factor of ~3 during the PETM and that excess burial took place in marginal marine to deep sea regions This would require increased Ba sourcing to the ocean. Although the source of Ba may be subject of discussion, the magnitude of change is larger, and the time scale of response shorter than can be achieved within the commonly accepted time scale and magnitude of increased weathering. Although outstanding issues regarding the transport of Ba to open ocean sediments remain, we therefore consider massive dissolved Ba release from pore water below dissociating methane hydrates the most likely explanation. Combined with other circumstantial evidence, we argue methane hydrate dissociation likely acted as a strong positive carbon cycle feedback to warming.

The global warming prior to the injection of ^{13}C-depleted C is likely driven by a rise in greenhouse gas concentrations. Particularly because volcanic C input would only minimally affect global exogenic $\delta^{13}C$, we find

CO_2 input from the NAIP remains a plausible explanation. However, until better dating for the volcanic deposits, tracers for volcanic activity and/or volumetric assessments for the NAIP emerge, a sizeable volcanic pulse within this particular interval remains speculative. Similar issues hamper the assessment of an orbital trigger. While permafrost thawing may be invoked as C source to drive pre-CIE warming under favorable astronomical configurations, the available carbon volume is difficult to estimate and the release should be accompanied by a small, currently undetected, global $\delta^{13}C$ decrease.

Despite differences in background climate state and regardless of the underlying mechanism or CO_2 source, the observed surface warming in the last millennia of the Paleocene (~2 °C) is strikingly similar in magnitude to that projected for the coming centuries and our findings highlight the potential of strong positive carbon cycle feedbacks even under relatively low amplitude surface warming.

Acknowledgments
We thank the International Ocean Discovery Program (IODP) for access to materials and data; N. Welters, A. van Dijk, and D. Kasjaniuk (Utrecht) for analytical support; A. Wuelbers and W. Hale (IODP Bremen Core Repository) and W. Schinkel (Erasmus University Rotterdam) for sampling assistance; and E. van Nes (Wageningen University) for advice regarding statistical analyses. We thank S. Lyapunov (Geological Institute of Russian Academy of Sciences) for the geochemical data from the West Siberian Sea. The European Research Council (ERC) under the European Union Seventh Framework Program provided funding for this work by ERC Starting grant 259627 to A. Sluijs. The Netherlands Organization for Scientific Research (NWO) supported this work through grant 834.11.006 to G.-J. Reichart and J.S. Sinninghe Damsté. This work was carried out under the program of the Netherlands Earth System Science Centre (NESSC), financially supported by the Dutch Ministry of Education, Culture and Science (OCW). We thank Kate Littler and several anonymous reviewers for thoughtful and constructive reviews and Stephen Barker for editorial handling. Author contributions: J. F., A. S., and G. -J. R. designed the study. J. F., J. S. S. D., and F. P. performed organic geochemical analyses. J. F., S. M. B., and G. -J. R. performed inorganic geochemical analyses. D. J. L. ran HadCM3L experiments. All authors analyzed and discussed the data. J. F. and A. S. wrote the paper, with input from all authors. The authors declare no competing financial interests. Raw data used in this contribution can be found in the online database Pangaea (https://doi.pangaea.de/10.1594/PANGAEA.899283). Other requests for materials and correspondence to: J. F. (j.frieling1@uu.nl). References used in supporting information files (not used in main text; Cramer et al., 1999; Frieling et al., 2014; Gibbs et al., 2006; John et al., 2008; Kelly et al., 2012; Nomura & Takata, 2005; Sluijs et al., 2006; Sluijs & Brinkhuis, 2009; Stassen et al., 2012).

References

Agnini, C., Macrì, P., Backman, J., Brinkhuis, H., Fornaciari, E., Giusberti, L., et al. (2009). An early Eocene carbon cycle perturbation at ~52.5 Ma in the Southern Alps: Chronology and biotic response. *Paleoceanography*, *24*, PA2209. https://doi.org/10.1029/2008PA001649

Algeo, T. J., Luo, G. M., Song, H. Y., Lyons, T. W., & Canfield, D. E. (2015). Reconstruction of secular variation in seawater sulfate concentrations. *Biogeosciences*, *12*(7), 2131–2151. https://doi.org/10.5194/bg-12-2131-2015

Archer, D., & Buffett, B. (2005). Time-dependent response of the global ocean clathrate reservoir to climatic and anthropogenic forcing. *Geochemistry, Geophysics, Geosystems*, *6*, Q03002. https://doi.org/10.1029/2004GC000854

Archer, D., Buffett, B., & Brovkin, V. (2009). Ocean methane hydrates as a slow tipping point in the global carbon cycle. *Proceedings of the National Academy of Sciences*, *106*(49), 20,596–20,601. https://doi.org/10.1073/pnas.0800885105

Babila, T. L., Rosenthal, Y., Wright, J. D., & Miller, K. G. (2016). A continental shelf perspective of ocean acidification and temperature evolution during the Paleocene-Eocene thermal maximum. *Geology*, *44*(4), G37522.1. https://doi.org/10.1130/G37522.1

Bains, S., Norris, R. D., Corfield, R. M., & Faul, K. L. (2000). Termination of global warmth at the Palaeocene/Eocene boundary through productivity feedback. *Nature*, *407*(6801), 171–174. https://doi.org/10.1038/35025035

Beckmann, B., Flögel, S., Hofmann, P., Schulz, M., & Wagner, T. (2005). Orbital forcing of Cretaceous river discharge in tropical Africa and ocean response. *Nature*, *437*(7056), 241–244. https://doi.org/10.1038/nature03976

Bijl, P. K., Schouten, S., Sluijs, A., Reichart, G.-J., Zachos, J. C., & Brinkhuis, H. (2009). Early Palaeogene temperature evolution of the southwest Pacific Ocean. *Nature*, *461*(7265), 776–779. https://doi.org/10.1038/nature08399

Bornemann, A., Schulte, P., Sprong, J., Steurbaut, E., Youssef, M., & Speijer, R. P. (2009). Latest Danian carbon isotope anomaly and associated environmental change in the southern Tethys (Nile Basin, Egypt). *Journal of the Geological Society*, *166*(6), 1135–1142. https://doi.org/10.1144/0016-76492008-104

Carmichael, M. J., Inglis, G. N., Badger, M. P. S., Naafs, B. D. A., Behrooz, L., Remmelzwaal, S., et al. (2017). Hydrological and associated biogeochemical consequences of rapid global warming during the Paleocene-Eocene thermal maximum. *Global and Planetary Change*, *157*(August), 114–138. https://doi.org/10.1016/j.gloplacha.2017.07.014

Chen, Z., Wang, X., Hu, J., Yang, S., Zhu, M., Dong, X., et al. (2014). Structure of the carbon isotope excursion in a high-resolution lacustrine Paleocene–Eocene thermal maximum record from central China. *Earth and Planetary Science Letters*, *408*, 331–340. https://doi.org/10.1016/j.epsl.2014.10.027

Coccioni, R., Bancalà, G., Catanzarit, R., Fornaciari, E., Frontalini, F., Giusberti, L., et al. (2012). An integrated stratigraphic record of the Palaeocene-lower Eocene at Gubbio (Italy): New insights into the early Palaeogene hyperthermals and carbon isotope excursions. *Terra Nova*, *24*(5), 380–386. https://doi.org/10.1111/j.1365-3121.2012.01076.x

Cramer, B. S., Aubry, M.-P., Miller, K. G., Olsson, R. K., Wright, J. D., & Kent, D. V. (1999). An exceptional chronologic, isotopic, and clay mineralogic record of the latest Paleocene thermal maximum, Bass River, NJ, ODP 174AX. *Bulletin de la Societe Geologique de France*, *170*(6), 883–897.

Cramer, B. S., Wright, J. D., Kent, D. V., & Aubry, M.-P. (2003). Orbital climate forcing of d13C excursions in the late Paleocene-early Eocene (chrons C24n-C25n). *Paleoceanography*, *18*(4), 1097. https://doi.org/10.1029/2003PA000909 Retrieved from http://www.scopus.com/inward/record.url?eid=2-s2.0-1642357632&partnerID=40&md5=e225c616d2870c017d457b320c7144a2

Cramwinckel, M. J., Huber, M., Kocken, I. J., Agnini, C., Bijl, P. K., Bohaty, S. M., et al. (2018). Synchronous tropical and polar temperature evolution in the Eocene. *Nature*, *559*(7714), 382–386. https://doi.org/10.1038/s41586-018-0272-2

Crouch, E. M. (2001). *Environmental change at the time of the Paleocene-Eocene Biotic Turnover* (Doctoral dissertation). Utrecht University, Utrecht, The Netherlands.

DeConto, R. M., Galeotti, S., Pagani, M., Tracy, D., Schaefer, K., Zhang, T., et al. (2012). Past extreme warming events linked to massive carbon release from thawing permafrost. *Nature*, *484*(7392), 87–91. https://doi.org/10.1038/nature10929

Dehairs, F., Baeyens, W., & Goeyens, L. (1992). Accumulation of suspended barite at mesopelagic depths and export production in the Southern Ocean. *Science*, *258*(5086), 1332–1335. https://doi.org/10.1126/science.258.5086.1332

Deprez, A., Jehle, S., Bornemann, A., & Speijer, R. P. (2017). Pronounced biotic and environmental change across the latest Danian warming event (LDE) at Shatsky Rise, Pacific Ocean (ODP Site 1210). *Marine Micropaleontology*, *137*(February), 31–45. https://doi.org/10.1016/j.marmicro.2017.10.001

Dickens, G. R. (2001a). Carbon addition and removal during the late Palaeocene thermal maximum: Basic theory with a preliminary treatment of the isotope record at ODP Site 1051, Blake Nose. *Geological Society, London, Special Publications*, *183*(1), 293–305. https://doi.org/10.1144/GSL.SP.2001.183.01.14

Dickens, G. R. (2001b). The potential volume of oceanic methane hydrates with variable external conditions. *Organic Geochemistry*, *32*(10), 1179–1193. https://doi.org/10.1016/S0146-6380(01)00086-9

Dickens, G. R., Castillo, M. M., & Walker, J. C. G. (1997). A blast of gas in the latest Paleocene: Simulating first-order effects of massive dissociation on oceanic methane hydrate. *Geology*, *25*(3), 259–262. Retrieved fromhttp://www.scopus.com/inward/record.url?eid=2-s2.0-0030758008&partnerID=40&md5=a352de7c7989ca07a75de4e67be14b7a. https://doi.org/10.1130/0091-7613(1997)025<0259:ABOGIT>2.3.CO;2

Dickens, G. R., Fewless, T., Thomas, E., & Bralower, T. J. (2003). Excess barite accumulation during the Paleocene-Eocene thermal maximum: Massive input of dissolved barium from seafloor gas hydrate reservoirs. *Geological Society of America Special Papers*, *369*, 11–24. https://doi.org/10.1130/0-8137-2369-8.11

Dickens, G. R., O'Neil, J. R., Rea, D. K., & Owen, R. M. (1995). Dissociation of oceanic methane hydrate as a cause of the carbon isotope excursion at the end of the Paleocene. *Paleoceanography*, *10*(6), 965–971. https://doi.org/10.1029/95PA02087

Dickson, A. J., Cohen, A. S., & Coe, A. L. (2012). Seawater oxygenation during the Paleocene-Eocene thermal maximum. *Geology*, *40*(7), 639–642. https://doi.org/10.1130/G32977.1

Dickson, A. J., Cohen, A. S., Coe, A. L., Davies, M., Shcherbinina, E. A., & Gavrilov, Y. O. (2015). Evidence for weathering and volcanism during the PETM from Arctic Ocean and Peri-Tethys osmium isotope records. *Palaeogeography, Palaeoclimatology, Palaeoecology*, *438*, 300–307. https://doi.org/10.1016/j.palaeo.2015.08.019

Dunkley Jones, T., Lunt, D. J., Schmidt, D. N., Ridgwell, A. J., Sluijs, A., Valdes, P. J., & Maslin, M. A. (2013). Climate model and proxy data constraints on ocean warming across the Paleocene–Eocene thermal maximum. *Earth-Science Reviews*, *125*, 123–145. https://doi.org/ https://doi.org/10.1016/j.earscirev.2013.07.004

Dymond, J., Suess, E., & Lyle, M. (1992). Barium in Deep-Sea Sediment: A Geochemical Proxy for Paleoproductivity. *Paleoceanography*, *7*(2), 163–181. https://doi.org/10.1029/92PA00181

Eldholm, O., & Grue, K. (1994). North Atlantic volcanic margins: Dimensions and production rates. *Journal of Geophysical Research*, *99*(B2), 2955–2968. https://doi.org/10.1029/93JB02879

Eldholm, O., & Thomas, E. (1993). Environmental impact of volcanic margin formation. *Earth and Planetary Science Letters*, *117*(3-4), 319–329. https://doi.org/10.1016/0012-821X(93)90087-P

Farley, K., & Eltgroth, S. F. (2003). An alternative age model for the Paleocene–Eocene thermal maximum using extraterrestrial 3 He. *Earth and Planetary Science Letters*, *208*(3-4), 135–148. https://doi.org/10.1016/S0012-821X(03)00017-7

Frieling, J., Gebhardt, H., Huber, M., Adekeye, O. A., Akande, S. O., Reichart, G.-J., et al. (2017). Extreme warmth and heat-stressed plankton in the tropics during the Paleocene-Eocene thermal maximum. *Science Advances*, *3*(3), e1600891. https://doi.org/10.1126/sciadv.1600891

Frieling, J., Iakovleva, A. I., Reichart, G.-J., Aleksandrova, G. N., Gnibidenko, Z. N., Schouten, S., & Sluijs, A. (2014). Paleocene-Eocene warming and biotic response in the epicontinental West Siberian Sea. *Geology*, *42*(9), 767–770. https://doi.org/10.1130/G35724.1

Frieling, J., Reichart, G.-J., Middelburg, J. J., Röhl, U., Westerhold, T., Bohaty, S. M., & Sluijs, A. (2018). Tropical Atlantic climate and ecosystem regime shifts during the Paleocene–Eocene thermal maximum. *Climate of the Past*, *14*(1), 39–55. https://doi.org/10.5194/cp-14-39-2018

Frieling, J., Svensen, H. H., Planke, S., Cramwinckel, M. J., Selnes, H., & Sluijs, A. (2016). Thermogenic methane release as a cause for the long duration of the PETM. *Proceedings of the National Academy of Sciences*, *113*(43), 12,059–12,064. https://doi.org/10.1073/pnas.1603348113

Gehler, A., Gingerich, P. D., & Pack, A. (2016). Temperature and atmospheric CO_2 concentration estimates through the PETM using triple oxygen isotope analysis of mammalian bioapatite. *Proceedings of the National Academy of Sciences*, *113*, 7739–7744. https://doi.org/10.1073/pnas.1518116113

Gibbs, S. J., Bralower, T. J., Bown, P. R., Zachos, J. C., & Bybell, L. M. (2006). Shelf and open-ocean calcareous phytoplankton assemblages across the Paleocene-Eocene thermal maximum: Implications for global productivity gradients. *Geology*, *34*(4), 233. https://doi.org/10.1130/G22381.1

Gutjahr, M., Ridgwell, A., Sexton, P. F., Anagnostou, E., Pearson, P. N., Pälike, H., et al. (2017). Very large release of mostly volcanic carbon during the Palaeocene–Eocene thermal maximum. *Nature*, *548*(7669), 573–577. https://doi.org/10.1038/nature23646

Hall, J. M., Zachos, J. C., & Turekian, K. K. (2004). Barium cycling during the Paleocene-Eocene thermal maximum: Evidence from Ba/Ca in foraminifera. *Eos Transactions. AGU*, 85(47), Fall Meeting Supplement, Abstract PP14A-05.

Hollis, C. J., Dickens, G. R., Field, B. D., Jones, C. M., & Percy Strong, C. (2005). The Paleocene–Eocene transition at Mead Stream, New Zealand: A southern Pacific record of early Cenozoic global change. *Palaeogeography, Palaeoclimatology, Palaeoecology*, *215*, 313–343.

Hopmans, E. C., Schouten, S., & Sinninghe Damsté, J. S. (2016). The effect of improved chromatography on GDGT-based palaeoproxies. *Organic Geochemistry*, *93*, 1–6. https://doi.org/10.1016/j.orggeochem.2015.12.006

Hopmans, E. C., Weijers, J. W. H., Schefuß, E., Herfort, L., Sinninghe Damsté, J. S., & Schouten, S. (2004). A novel proxy for terrestrial organic matter in sediments based on branched and isoprenoid tetraether lipids. *Earth and Planetary Science Letters*, *224*(1–2), 107–116. https://doi.org/10.1016/j.epsl.2004.05.012

Imbert, P., & Ho, S. (2012). Seismic-scale funnel-shaped collapse features from the Paleocene-Eocene of the North West Shelf of Australia. *Marine Geology*, *332*, 198–221. https://doi.org/10.1016/j.margeo.2012.10.010

Inglis, G. N., Farnsworth, A., Lunt, D. J., Foster, G. L., Hollis, C. J., Pagani, M., et al. (2015). Descent towards the Icehouse: Eocene sea surface cooling inferred from GDGT distributions. *Paleoceanography*, *30*, 1000–1020. https://doi.org/10.1002/2014PA002723

IPCC (2014). Climate change 2014: Synthesis report. In Core Writing Team, R. K. Pachauri, & L. A. Meyer (Eds.), *Contribution of working groups I, II and III to the fifth assessment report of the intergovernmental panel on climate change* (p. 151). Geneva, Switzerland: IPCC.

John, C. M., Bohaty, S. M., Zachos, J. C., Sluijs, A., Gibbs, S. J., Brinkhuis, H., & Bralower, T. J. (2008). North American continental margin records of the Paleocene-Eocene thermal maximum: Implications for global carbon and hydrological cycling. *Paleoceanography*, *23*, PA2217. https://doi.org/10.1029/2007PA001465

John, E. H., Pearson, P. N., Coxall, H. K., Birch, H., Wade, B. S., & Foster, G. L. (2013). Warm ocean processes and carbon cycling in the Eocene. *Philosophical Transactions of the Royal Society A: Mathematical, Physical and Engineering Sciences*, *371*(2001), 20130099. https://doi.org/10.1098/rsta.2013.0099

Jones, M. T., Percival, L. M. E., Stokke, E. W., Frieling, J., Mather, T. A., Riber, L., et al. (2019). Mercury anomalies across the Palaeocene–Eocene thermal maximum. *Climate of the Past*, *15*(1), 217–236. https://doi.org/10.5194/cp-15-217-2019

Katz, M. E., Cramer, B. S., Mountain, G. S., Katz, S., & Miller, K. G. (2001). Uncorking the bottle: What triggered the Paleocene/Eocene thermal maximum methane release? *Paleoceanography*, *16*(6), 549–562. https://doi.org/10.1029/2000PA000615

Katz, M. E., Pak, D. K., Dickens, G. R., & Miller, K. G. (1999). The source and fate of massive carbon input during the latest Paleocene thermal maximum. *Science*, *286*(5444), 1531–1533. https://doi.org/10.1126/science.286.5444.1531

Kelly, D. C., Nielsen, T. M. J., & Schellenberg, S. A. (2012). Carbonate saturation dynamics during the Paleocene-Eocene thermal maximum: Bathyal constraints from ODP sites 689 and 690 in the Weddell Sea (South Atlantic). *Marine Geology*, *303–306*, 75–86. https://doi.org/10.1016/j.margeo.2012.02.003

Kennett, J. P., & Stott, L. D. (1991). Abrupt deep-sea warming, palaeoceanographic changes and benthic extinctions at the end of the Palaeocene. *Nature*, *353*, 225–229. https://doi.org/10.1038/353225a0

Kent, D. V., Cramer, B. S., Lanci, L., Wang, D., Wright, J. D., & Van der Voo, R. (2003). A case for a comet impact trigger for the Paleocene/Eocene thermal maximum and carbon isotope excursion. *Earth and Planetary Science Letters*, *211*(1–2), 13–26. https://doi.org/10.1016/S0012-821X(03)00188-2

Kim, J. H., van der Meer, J., Schouten, S., Helmke, P., Willmott, V., Sangiorgi, F., et al. (2010). New indices and calibrations derived from the distribution of crenarchaeal isoprenoid tetraether lipids: Implications for past sea surface temperature reconstructions. *Geochimica et Cosmochimica Acta*, *74*(16), 4639–4654. https://doi.org/10.1016/j.gca.2010.05.027

Kim, S.-T., & O'Neil, J. R. (1997). Equilibrium and nonequilibrium oxygen isotope effects in synthetic carbonates. *Geochimica et Cosmochimica Acta*, *61*(16), 3461–3475. https://doi.org/10.1016/S0016-7037(97)00169-5

Kirtland Turner, S., Hull, P., Kump, L., & Ridgwell, A. (2017). A probabilistic assessment of the rapidity of the PETM onset. *Nature Communications*, 1–9. https://doi.org/10.1038/s41467-017-00292-2

Kopp, R. E., Schumann, D., Raub, T. D., Powars, D. S., Godfrey, L. V., Swanson-Hysell, N. L., et al. (2009). An Appalachian Amazon? Magnetofossil evidence for the development of a tropical river-like system in the mid-Atlantic United States during the Paleocene-Eocene thermal maximum. *Paleoceanography*, *24*, PA4211. https://doi.org/10.1029/2009PA001783

Kump, L. R., & Arthur, M. A. (1999). Interpreting carbon-isotope excursions: Carbonates and organic matter. *Chemical Geology*, *161*(1-3), 181–198. https://doi.org/10.1016/S0009-2541(99)00086-8

Kurtz, A. C., Kump, L. R., Arthur, M. A., Zachos, J. C., & Paytan, A. (2003). Early Cenozoic decoupling of the global carbon and sulfur cycles. *Paleoceanography*, *18*(4), 1090. https://doi.org/10.1029/2003PA000908

Kvenvolden, K. A. (2002). Methane hydrate in the global organic carbon cycle. *Terra Nova*, *14*(5), 302–306. https://doi.org/10.1046/j.1365-3121.2002.00414.x

Lauretano, V., Hilgen, F. J., Zachos, J. C., & Lourens, L. J. (2016). Astronomically tuned age model for the early Eocene carbon isotope events: A new high-resolution delta C-13(benthic) record of ODP Site 1263 between ~ 49 and ~ 54 Ma. *Newsletters on Stratigraphy*, *49*(2), 383–400. https://doi.org/10.1127/nos/2016/0077

Lauretano, V., Littler, K., Polling, M., Zachos, J. C., & Lourens, L. J. (2015). Frequency, magnitude and character of hyperthermal events at the onset of the early Eocene climatic optimum. *Climate of the Past*, *11*(10), 1313–1324. https://doi.org/10.5194/cp-11-1313-2015

Littler, K., Röhl, U., Westerhold, T., & Zachos, J. C. (2014). A high-resolution benthic stable-isotope record for the South Atlantic: Implications for orbital-scale changes in late Paleocene–early Eocene climate and carbon cycling. *Earth and Planetary Science Letters*, *401*, 18–30. https://doi.org/10.1016/j.epsl.2014.05.054

Lourens, L. J., Sluijs, A., Kroon, D., Zachos, J. C., Thomas, E., Röhl, U., et al. (2005). Astronomical pacing of late Palaeocene to early Eocene global warming events. *Nature*, *435*(7045), 1083–1087. Retrieved from http://www.scopus.com/inward/record.url?eid=2-s2.0-21344435540&partnerID=40&md5=79798ae44067798027e5569333851687. https://doi.org/10.1038/nature03814

Lowenstein, T. K., Timofeeff, M. N., Brennan, S. T., Hardie, L. A., & Demicco, R. V. (2001). Oscillations in Phanerozoic seawater chemistry: Evidence from fluid inclusions. *Science*, *294*(5544), 1086–1088. https://doi.org/10.1126/science.1064280

Lunt, D. J., Dunkley Jones, T., Heinemann, M., Huber, M., LeGrande, A. N., Winguth, A. M. E., et al. (2012). A model–data comparison for a multi-model ensemble of early Eocene atmosphere–ocean simulations: EoMIP. *Climate of the Past*, *8*, 1717–1736. https://doi.org/10.5194/cp-8-1717-2012

Lunt, D. J., Ridgwell, A. J., Sluijs, A., Zachos, J. C., Hunter, S., & Haywood, A. M. (2011). A model for orbital pacing of methane hydrate destabilization during the Palaeogene. *Nature Geoscience*, *4*(11), 775–778. https://doi.org/10.1038/ngeo1266

Lunt, D. J., Valdes, P. J., Jones, T. D., Ridgwell, A. J., Haywood, A. M., Schmidt, D. N., et al. (2010). CO_2-driven ocean circulation changes as an amplifier of Paleocene-Eocene thermal maximum hydrate destabilization. *Geology*, *38*(10), 875–878. https://doi.org/10.1130/G31184.1

Lyons, S. L., Baczynski, A. A., Babila, T. L., Bralower, T. J., Hajek, E. A., Kump, L. R., et al. (2019). Palaeocene–Eocene thermal maximum prolonged by fossil carbon oxidation. *Nature Geoscience*, *12*(1), 54–60. https://doi.org/10.1038/s41561-018-0277-3

Ma, Z., Gray, E., Thomas, E., Murphy, B., Zachos, J. C., & Paytan, A. (2014). Carbon sequestration during the Palaeocene–Eocene thermal maximum by an efficient biological pump. *Nature Geoscience*, *7*(May), 382–388. https://doi.org/10.1038/ngeo2139

März, C., Schnetger, B., & Brumsack, H.-J. (2010). Paleoenvironmental implications of Cenozoic sediments from the central Arctic Ocean (IODP Expedition 302) using inorganic geochemistry. *Paleoceanography*, *25*, PA3206. https://doi.org/10.1029/2009PA001860

McInerney, F. A., & Wing, S. L. (2011). The Paleocene-Eocene thermal maximum: A perturbation of carbon cycle, climate, and biosphere with implications for the future. *Annual Review of Earth and Planetary Sciences*, *39*, 489–516. https://doi.org/10.1146/annurev-earth-040610-133431

Meissner, K. J., Bralower, T. J., Alexander, K., Jones, T. D., Sijp, W., & Ward, M. (2014). The Paleocene-Eocene thermal maximum: How much carbon is enough? *Paleoceanography*, *29*, 946–963. https://doi.org/10.1002/2014PA002650

Morgan, J. P., Reston, T. J., & Ranero, C. R. (2004). Contemporaneous mass extinctions, continental flood basalts, and 'impact signals': Are mantle plume-induced lithospheric gas explosions the causal link? *Earth and Planetary Science Letters*, *217*(3-4), 263–284. https://doi.org/10.1016/S0012-821X(03)00602-2

Murphy, B. H., Farley, K., & Zachos, J. C. (2010). An extraterrestrial 3 He-based timescale for the Paleocene–Eocene thermal maximum (PETM) from Walvis Ridge, IODP Site 1266. *Geochimica et Cosmochimica Acta*, *74*(17), 5098–5108. https://doi.org/10.1016/j.gca.2010.03.039

Nisbet, E. G., Jones, S. M., Maclennan, J., Eagles, G., Moed, J., Warwick, N., et al. (2009). Kick-starting ancient warming. *Nature Geoscience*, *2*(3), 156–159. https://doi.org/10.1038/ngeo454

Nomura, R., & Takata, H. (2005). Data report: Paleocene/Eocene Benthic Foraminifers, ODP Leg 199 Sites 1215, 1220, and 1221, Equatorial Central Pacific Ocean. In *Proceedings of the Ocean Drilling Program, Scientific Results* (Vol. 199, pp. 1–34). College Station, TX: Ocean Drilling Program.

Oboh-Ikuenobe, F. E., Yepes, O., Mascle, J., Lohmann, G. P., Clift, P., Akamaluk, T., et al. (1997). Palynofacies analysis of sediments from the Cote d'Ivoire-Ghana Transform Margin: Preliminary correlation with some regional events in the Equatorial Atlantic. *Palaeogeography, Palaeoclimatology, Palaeoecology*, *129*(3–4), 291–314. https://doi.org/10.1016/S0031-0182(96)00125-3

PALAEOSENS (2012). Making sense of palaeoclimate sensitivity. *Nature*, *491*(7426), 683–691. https://doi.org/10.1038/nature11574

Pälike, C., Delaney, M. L., & Zachos, J. C. (2014). Deep-sea redox across the Paleocene-Eocene thermal maximum. *Geochemistry, Geophysics, Geosystems*, *15*, 1038–1053. https://doi.org/10.1002/2013GC005074

Panchuk, K., Ridgwell, A. J., & Kump, L. R. (2008). Sedimentary response to Paleocene-Eocene thermal maximum carbon release: A model-data comparison. *Geology*, *36*(4), 315–318. https://doi.org/10.1130/G24474A.1

Party, S. S. (1996). Site 959. In J. Mascle, G. P. Lohmann, P. D. Clift, et al. (Eds.), *Proceedings of the Ocean Drilling Program, Initial Reports* (Vol. 159, pp. 65–150). College Station, TX: Ocean Drilling Program.

Paytan, A., Averyt, K., Faul, K., Gray, E., & Thomas, E. (2007). Barite accumulation, ocean productivity, and Sr/Ba in barite across the Paleocene–Eocene thermal maximum. *Geology*, *35*(12), 1139–1142. https://doi.org/10.1130/G24162A.1

Pearson, P. N. (2017). Sediment creep, mixing, symbiont bleaching and diagenesis: Reinterpretation of the Paleocene/Eocene boundary stable isotope records at ODP Sites 689 and 690, Maud Rise. In *Climatic and Biotic Events of the Paleogene* (p. 73).

Penman, D. E. (2016). Silicate weathering and North Atlantic silica burial during the Paleocene-Eocene thermal maximum. *Geology*, *9*, G37704.1. https://doi.org/10.1130/G37704.1

Penman, D. E., Hönisch, B., Zeebe, R. E., Thomas, E., & Zachos, J. C. (2014). Rapid and sustained surface ocean acidification during the Paleocene-Eocene thermal maximum. *Paleoceanography*, *29*, 357–369. https://doi.org/10.1002/2014PA002621

Quattlebaum, T. (2004). The environmental impact of the paleocene-eocene thermal maximum on the coastal ocean: a multi-proxy approach. University of California, Santa Cruz.

Ravizza, G., Norris, R. D., Blusztajn, J., & Aubry, M.-P. (2001). An osmium isotope excursion associated with the late Paleocene thermal maximum: Evidence of intensified chemical weathering. *Paleoceanography*, *16*(2), 155–163. https://doi.org/10.1029/2000PA000541

Reitz, A., Pfeifer, K., De Lange, G. J., & Klump, J. (2004). Biogenic barium and the detrital Ba/Al ratio: A comparison of their direct and indirect determination. *Marine Geology*, *204*(3-4), 289–300. https://doi.org/10.1016/S0025-3227(04)00004-0

Röhl, U., Westerhold, T., Bralower, T. J., & Zachos, J. C. (2007). On the duration of the Paleocene-Eocene thermal maximum (PETM). *Geochemistry, Geophysics, Geosystems*, *8*, Q12002. https://doi.org/10.1029/2007GC001784

Rutsch, H.-J. J., Mangini, A., Bonani, G., Dittrich-Hannen, B., Kubik, P. W., Suter, M., & Segl, M. (1995). 10Be and Ba concentrations in West African sediments trace productivity in the past. *Earth and Planetary Science Letters*, *133*(1–2), 129–143. https://doi.org/10.1016/0012-821X(95)00069-O

Schmitz, B., Peucker-Ehrenbrink, B., Heilmann-Clausen, C., Aberg, G., Asaro, F., & Lee, C.-T. A. (2004). Basaltic explosive volcanism, but no comet impact, at the Paleocene–Eocene boundary: High-resolution chemical and isotopic records from Egypt, Spain and Denmark. *Earth and Planetary Science Letters*, *225*(1-2), 1–17. https://doi.org/10.1016/j.epsl.2004.06.017

Schouten, S., Huguet, C., Hopmans, E. C., Kienhuis, M. V. M., & Sinninghe Damsté, J. S. (2007). Analytical methodology for TEX 86 Paleothermometry by high-performance liquid chromatography/atmospheric pressure chemical ionization-mass spectrometry. *Analytical Chemistry*, *79*(7), 2940–2944. https://doi.org/10.1021/ac062339v

Secord, R., Gingerich, P. D., Lohmann, K. C., & MacLeod, K. G. (2010). Continental warming preceding the Palaeocene-Eocene thermal maximum. *Nature*, *467*(7318), 955–958. https://doi.org/10.1038/nature09441

Self, S., Widdowson, M., Thordarson, T., & Jay, A. E. (2006). Volatile fluxes during flood basalt eruptions and potential effects on the global environment: A Deccan perspective. *Earth and Planetary Science Letters*, *248*(1-2), 518–532. https://doi.org/10.1016/j.epsl.2006.05.041

Sexton, P. F., Norris, R. D., Wilson, P. A., Pälike, H., Westerhold, T., Röhl, U., et al. (2011). Eocene global warming events driven by ventilation of oceanic dissolved organic carbon. *Nature*, *471*(7338), 349–352. https://doi.org/10.1038/nature09826

Shafik, S., Watkins, D. K., & Shin, I. C. (1998). 32. Calcareous Nannofossil Paleogene Biostratigraphy, Côte D' Ivoire-Ghana. *Proceeding of the Ocean Drilling Program, Scientific Results*, *159*(1985), 413–431.

Siever, R. (1991). Silica in the oceans: Biological-geochemical interplay. In S. Schneider & P. Boston (Eds.), *Scientists on Gaia* (pp. 287–295). Cambridge, MA: MIT Press.

Sinninghe Damsté, J. S., Ossebaar, J., Schouten, S., & Verschuren, D. (2012). Distribution of tetraether lipids in the 25-ka sedimentary record of Lake Challa: Extracting reliable TEX 86 and MBT/CBT palaeotemperatures from an equatorial African lake. *Quaternary Science Reviews*, *50*, 43–54. https://doi.org/10.1016/j.quascirev.2012.07.001

Sluijs, A., & Brinkhuis, H. (2009). A dynamic climate and ecosystem state during the Paleocene-Eocene thermal maximum—Inferences from dinoflagellate cyst assemblages at the New Jersey Shelf. *Biogeosciences*, *6*(8), 1755–1781. https://doi.org/10.5194/bg-6-1755-2009

Sluijs, A., Brinkhuis, H., Schouten, S., Bohaty, S. M., John, C. M., Zachos, J. C., et al. (2007). Environmental precursors to rapid light carbon injection at the Palaeocene/Eocene boundary. *Nature*, *450*(7173), 1218–1221. https://doi.org/10.1038/nature06400

Sluijs, A., & Dickens, G. R. (2012). Assessing offsets between the δ 13 C of sedimentary components and the global exogenic carbon pool across early Paleogene carbon cycle perturbations. *Global Biogeochemical Cycles*, *26*, GB4005. https://doi.org/10.1029/2011GB004224

Sluijs, A., Schouten, S., Pagani, M., Woltering, M., Brinkhuis, H., Sinninghe Damsté, J. S., et al. (2006). Subtropical Arctic Ocean temperatures during the Palaeocene/Eocene thermal maximum. *Nature*, *441*(7093), 610–613. https://doi.org/10.1038/nature04668

Sluijs, A., Van Roij, L., Harrington, G. J., Schouten, S., Sessa, J. A., Levay, L. J., et al. (2014). Warming, euxinia and sea level rise during the paleocene-eocene thermal maximum on the gulf coastal plain: Implications for ocean oxygenation and nutrient cycling. *Climate of the Past*, *10*(4), 1421–1439. https://doi.org/10.5194/cp-10-1421-2014

Soliman, M. F. (2003). Chemostratigraphy of the Paleocene/Eocene (P/E) boundary sediments at Gabal el-Qreiya, Nile Valley, Egypt. *Micropaleontology*, *49*(Suppl_1), 123–138. https://doi.org/10.2113/49.Suppl_1.123

Soliman, M. F., Aubry, M.-P., Schmitz, B., & Sherrell, R. M. (2011). Enhanced coastal paleoproductivity and nutrient supply in upper Egypt during the Paleocene/Eocene thermal maximum (PETM): Mineralogical and geochemical evidence. *Palaeogeography, Palaeoclimatology, Palaeoecology*, *310*(3–4), 365–377. https://doi.org/10.1016/j.palaeo.2011.07.027

Stassen, P., Thomas, E., & Speijer, R. P. (2012). Integrated stratigraphy of the Paleocene-Eocene thermal maximum in the New Jersey Coastal Plain: Toward understanding the effects of global warming in a shelf environment. *Paleoceanography*, *27*, PA4210. https://doi.org/10.1029/2012PA002323

Stoll, H. M. (2005). Limited range of interspecific vital effects in coccolith stable isotopic records during the Paleocene-Eocene thermal maximum. *Paleoceanography*, *20*, PA1007. https://doi.org/10.1029/2004PA001046

Storey, M., Duncan, R. A., & Swisher, C. C. (2007). Paleocene-Eocene thermal maximum and the opening of the Northeast Atlantic. *Science*, *316*(5824), 587–589. https://doi.org/10.1126/science.1135274

Svensen, H., Planke, S., Maithe-Sørensen, A., Jamtveit, B., Myklebust, R., Eidem, T. R., & Rey, S. S. (2004). Release of methane from a volcanic basin as a mechanism for initial Eocene global warming. *Nature*, *429*(6991), 542–545. Retrieved from http://www.scopus.com/inward/record.url?eid=2-s2.0-2942567617&partnerID=40&md5=4df8659bf3d920d6def6b0b509904880. https://doi.org/10.1038/nature02566

Thomas, D. J., Zachos, J. C., Bralower, T. J., Thomas, E., & Bohaty, S. M. (2002). Warming the fuel for the fire: Evidence for the thermal dissociation of methane hydrate during the Paleocene-Eocene thermal maximum dissociation of methane hydrate during the Paleocene-Eocene. *Geology*, *30*(12), 1067–1070. https://doi.org/10.1130/0091-7613(2002)030<1067:WTFFTF>2.0.CO;2

Tierney, J. E., & Tingley, M. P. (2014). A Bayesian, spatially-varying calibration model for the TEX86 proxy. *Geochimica et Cosmochimica Acta*, *127*(November), 83–106. https://doi.org/10.1016/j.gca.2013.11.026

Turgeon, S. C., & Creaser, R. A. (2008). Cretaceous oceanic anoxic event 2 triggered by a massive magmatic episode. *Nature*, *454*(7202), 323–326. https://doi.org/10.1038/nature07076

Uchikawa, J., & Zeebe, R. E. (2010). Examining possible effects of seawater pH decline on foraminiferal stable isotopes during the Paleocene-Eocene thermal maximum. *Paleoceanography*, *25*, PA2216. https://doi.org/10.1029/2009PA001864

Valentine, D. L., Blanton, D. C., Reeburgh, W. S., & Kastner, M. (2001). Water column methane oxidation adjacent to an area of active hydrate dissociation, Eel River Basin. *Geochimica et Cosmochimica Acta*, *65*(16), 2633–2640. https://doi.org/10.1016/S0016-7037(01)00625-1

Wagner, T. (2002). Late cretaceous to early Quaternary organic sedimentation in the eastern Equatorial Atlantic. *Palaeogeography, Palaeoclimatology, Palaeoecology*, *179*(1-2), 113–147. https://doi.org/10.1016/S0031-0182(01)00415-1

Wehausen, R., & Brumsack, H. J. (1998). 17. The formation of Pliocene Mediterranean Sapropels: Constraints from high-resolution major and minor element studies. *Proceeding of the Ocean Drilling Program, Scientific Results*, *160*, 207–217.

Weijers, J. W. H., Lim, K. L. H., Aquilina, A., Damsté, J. S. S., & Pancost, R. D. (2011). Biogeochemical controls on glycerol dialkyl glycerol tetraether lipid distributions in sediments characterized by diffusive methane flux. *Geochemistry, Geophysics, Geosystems*, *12*, Q10010. https://doi.org/10.1029/2011GC003724

Weijers, J. W. H., Schouten, S., Spaargaren, O. C., & Sinninghe Damsté, J. S. (2006). Occurrence and distribution of tetraether membrane lipids in soils: Implications for the use of the TEX86 proxy and the BIT index. *Organic Geochemistry*, *37*(12), 1680–1693. https://doi.org/10.1016/j.orggeochem.2006.07.018

Westerhold, T., & Röhl, U. (2009). High resolution cyclostratigraphy of the early Eocene—New insights into the origin of the Cenozoic cooling trend. *Climate of the Past Discussions*, *5*(3), 309–327. https://doi.org/10.5194/cp-5-309-2009

Westerhold, T., Röhl, U., Frederichs, T., Agnini, C., Raffi, I., Zachos, J. C., & Wilkens, R. H. (2017). Astronomical calibration of the Ypresian time scale: Implications for seafloor spreading rates and the chaotic behaviour of the solar system? *Climate of the Past Discussions*, 1–34. https://doi.org/10.5194/cp-2017-15

Wieczorek, R., Fantle, M. S., Kump, L. R., & Ravizza, G. (2013). Geochemical evidence for volcanic activity prior to and enhanced terrestrial weathering during the Paleocene Eocene thermal maximum. *Geochimica et Cosmochimica Acta*, *119*, 391–410. https://doi.org/10.1016/j.gca.2013.06.005

Wilkinson, C. M., Ganerød, M., Hendriks, B. W. H., & Eide, E. A. (2016). Compilation and appraisal of geochronological data from the North Atlantic Igneous Province (NAIP). *Geological Society, London, Special Publications*, SP447.10. https://doi.org/10.1144/SP447.10

Yasukawa, K., Nakamura, K., Fujinaga, K., Ikehara, M., & Kato, Y. (2017). Earth system feedback statistically extracted from the Indian Ocean deep-sea sediments recording Eocene hyperthermals. *Scientific Reports*, *7*(1), 11304. https://doi.org/10.1038/s41598-017-11470-z

Zachos, J. C., Bohaty, S. M., John, C. M., McCarren, H. K., Kelly, D. C., & Nielsen, T. M. J. (2007). The Palaeocene-Eocene carbon isotope excursion: Constraints from individual shell planktonic foraminifer records. *Philosophical Transactions. Series A, Mathematical, Physical, and Engineering Sciences*, *365*(1856), 1829–1842. https://doi.org/10.1098/rsta.2007.2045

Zachos, J. C., Dickens, G. R., & Zeebe, R. E. (2008). An early Cenozoic perspective on greenhouse warming and carbon-cycle dynamics. *Nature*, *451*(7176), 279–283. https://doi.org/10.1038/nature06588

Zachos, J. C., McCarren, H. K., Murphy, B., Röhl, U., & Westerhold, T. (2010). Tempo and scale of late Paleocene and early Eocene carbon isotope cycles: Implications for the origin of hyperthermals. *Earth and Planetary Science Letters*, *299*(1-2), 242–249. https://doi.org/10.1016/j.epsl.2010.09.004

Zachos, J. C., Rohl, U., Schellenberg, S. A., Sluijs, A., Hodell, D. A., Kelly, D. C., et al. (2005). Rapid acidification of the ocean during the Paleocene-Eocene thermal maximum. *Science*, *308*(5728), 1611–1615. https://doi.org/10.1126/science.1109004

Zachos, J. C., Stott, L. D., & Lohmann, K. C. (1994). Evolution of early Cenozoic marine temperatures at Equator. *Paleoceanography*, *9*(2), 353–387. https://doi.org/10.1029/93PA03266

Zeebe, R. E., Ridgwell, A., & Zachos, J. C. (2016). Anthropogenic carbon release rate unprecedented during the past 66 million years. *Nature Geoscience*, *9*(4), 325–329. https://doi.org/10.1038/ngeo2681

Zeebe, R. E., Zachos, J. C., & Dickens, G. R. (2009). Carbon dioxide forcing alone insufficient to explain Palaeocene–Eocene thermal maximum warming. *Nature Geoscience*, *2*(8), 576–580. https://doi.org/10.1038/ngeo578

Zhang, Y. G., Pagani, M., & Wang, Z. (2016). Ring Index: A new strategy to evaluate the integrity of TEX 86 paleothermometry. *Paleoceanography*, *31*, 220–232. https://doi.org/10.1002/2015PA002848

Zhang, Y. G., Zhang, C. L., Liu, X. L., Li, L., Hinrichs, K. U., & Noakes, J. E. (2011). Methane index: A tetraether archaeal lipid biomarker indicator for detecting the instability of marine gas hydrates. *Earth and Planetary Science Letters*, *307*(3–4), 525–534. https://doi.org/10.1016/j.epsl.2011.05.031

Zhou, X., Thomas, E., Winguth, A. M. E., Ridgwell, A., Scher, H., Hoogakker, B. A. A., et al. (2016). Expanded oxygen minimum zones during the late Paleocene-early Eocene: Hints from multiproxy comparison and ocean modeling. *Paleoceanography*, *31*, 1532–1546. https://doi.org/10.1002/2016PA003020